# Nondimensional parameter regimes of Arctic ice keel-ocean flow interactions

Fangchen Liu<sup>1</sup> and Varvara E. Zemskova<sup>1</sup>

This is a non-peer-reviewed preprint that has been submitted to *The Cryosphere*.

<sup>&</sup>lt;sup>1</sup>University of Waterloo, Department of Applied Mathematics, 200 University Ave W, Waterloo, ON N2L 3G1, Canada **Correspondence:** Varvara E. Zemskova (barbara.zemskova@uwaterloo.ca)

**Abstract.** Sea ice keels modulate upper-ocean momentum and mixing through internal wave (IW) generation, yet their effects are difficult to represent in climate models because their spatio-temporal scales are smaller than those of climate models and difficult to study in idealized simulations because geometry, forcing, and stratification span a large parameter space. We construct a compact description of the idealized representation of this problem by deriving five nondimensional parameters: lee-wave radiation potential  $(\chi)$ , IW nonlinearity (J), keel steepness  $(\zeta)$ , mixed-layer depth relative to keel draft  $(\eta)$ , and pycnocline strength (Ri). We then calculate these five nondimensional parameters over the Arctic Ocean using monthly data from NEMO-CICE model output over the 2000 - 2017 time period. After extracting only the data points that fall within the lee wave radiating range  $(0 < \chi < 1)$  and time-averaging, we apply the unsupervised Gausian Mixture Model (GMM) clustering to find regions with similar nondimensional parameter distributions. GMM reveals mechanically distinct, geographically coherent regions: boundary and marginal seas (Clusters 0-2) versus open-ocean regions that span from the central basin toward shelves (Clusters 3-5). The parameter regimes differ systematically in  $\eta$  and Ri: large  $\eta$  near boundaries implies weak keel-pycnocline coupling, whereas smaller  $\eta$  and steeper keels characterize the central Arctic regions. To diagnose dynamics, we run idealized two-dimensional nonhydrostatic numerical simulations with Boussinesq approximation with nondimensional parameters associated the mean values of each GMM cluster and quantify turbulent kinetic energy dissipation above, within, and below the pycnocline. The boundary regions (Clusters 0-1;  $\eta \approx 27-55$ ) show negligible IW and turbulence response below the pycnocline. The central Arctic regions with larger  $\zeta$  and J (Clusters 3 – 5) exhibit enhanced near-pycnocline turbulence, but downward energy propagation is limited where Ri is large ( $\sim$ 290–500) and increases in regions closer to shelves with a smaller Ri value ( $\sim$ 130). Recasting previous IW drag parameterization to a nondimensional form shows it is most sensitive to  $\eta$ , increasing sharply as  $\eta \to 0$  and weakly to Ri at fixed  $\eta$ . However, the results of our numerical simulations suggest that there may be some deviations from this parameterization that need to be further explored. Together, the nondimensional framework and clustering bound the physically relevant parameter space, identify where mixed-layer IW-drag parameterizations are credible, and provide concrete target ranges of nondimensional values to use in numerical simulations for calibration of the parameterizations.

## 25 1 Introduction

30

55

Sea ice keels, formed by rafting and overturning of pressure ridges, extend tens of meters below the surface, representing a crucial yet under-explored aspect of Arctic ice dynamics. Their morphology reflects past mechanical forcing—such as ice convergence and interactions with the ocean and the atmosphere (Kharitonov and Borodkin, 2020) —and exerts lasting influences on ocean processes beneath the ice, notably internal wave (IW) generation (Kawaguchi et al., 2019).

When drifting over a stratified ocean, keels act as moving topographic features that perturb density interfaces, generating IWs that radiate from the ice-ocean boundary and enhance momentum transfer (Flocco et al., 2024). This mechanism builds upon classical flow-topography interaction theory (Bell Jr., 1975), which originally assumed constant stratification. Significant modeling efforts have been dedicated to this problem (see e.g., review articles: Garrett and Kunze (2007); Legg (2021); e.g. theoretical and modeling studies: Nikurashin and Ferrari (2010); Klymak (2018); Perfect et al. (2020); Zemskova and Grisouard (2021); Baker and Mashayek (2022).)

However, Arctic stratification deviates from the assumptions of this classical theory, typically featuring a shallow mixed layer of cold and fresh water overlaying a sharp pycnocline that separates it from the stratified ocean interior. McPhee and Kantha (1989) extended the framework of flow interacting with a topographic feature to Arctic conditions by introducing a parameterization for the IW drag coefficient  $C_{\rm IW}$ , which depends on keel geometry, keel speed relative to the ocean currents' speed, and the strength and vertical position of the pycnocline. Depending on the magnitude of these parameters, it is possible for a keel to disturb the established stratification or penetrate the pycnocline directly, amplifying IW generation across both layers. Flocco et al. (2024) applied this parameterization to demonstrate via a coupled ice—ocean model that the resulting IW drag can reduce ice drift by up to 10%, enhance sea ice thickness by as much as 15% in regions such as the Canadian Arctic, and suppress bottom melt rates.

Beyond IW generation, keels actively stir the upper ocean, modulating stratification and mixed-layer depths through turbulence and vortex shedding. Large-eddy simulations show that keels can amplify vertical heat fluxes by factors of 3 – 10 (Skyllingstad et al., 2003). One of the key control nondimensional parameters governing this problem is the Froude number, Fr =  $\frac{u_0}{\sqrt{z_0 \, \Delta b}}$  (where  $u_0$  is the keel speed relative to the ocean currents,  $z_0$  is the mixed layer depth, and  $\Delta b$  is the buoyancy jump across the pycnocline), which compares keel speed to the internal wave phase speed. De Abreu et al. (2024) explored Fr = 0.5 – 2.0 range, spanning subcritical to supercritical regimes, and found that mixing strength and vertical extent vary non-monotonically with Fr and keel draft, peaking under specific vortex-shedding conditions. Similarly, Zhang et al. (2022) showed that under-ice flows around floe edges and keels can generate secondary IWs and trigger overturning. Together, these findings underscore the critical role of sea ice morphology in regulating upper-ocean stratification and highlight the need for its accurate representation in coupled climate models.

Despite their importance, accurately representing the impact of sea ice keels in climate models is challenging due to the broad parameter space involved, encompassing diverse keel geometries, oceanic stratification conditions, and flow characteristics. Observed keel sizes — typically on the order of tens of meters (Metzger et al., 2021) — are significantly smaller than the horizontal grid resolution of current global climate models (Selivanova et al., 2024), necessitating careful parameterization.

Even the high-resolution global climate models have horizontal grid spacing of about  $0.25^{\circ}$ , which at  $70^{\circ}$ N corresponds to roughly 10 km, that is two orders of magnitude larger than typical keel dimensions. Modern climate models still exhibit large uncertainties regarding projections of the Arctic sea ice state (e.g., Notz and Community, 2020; Rosenblum et al., 2021; Bouchat et al., 2022; Hutter et al., 2022) and one of the main current recommendations is to improve our understanding and parameterization of sea ice physics rather than running climate models at significantly higher resolution (Selivanova et al., 2024). Existing theoretical frameworks, such as the parameterization by McPhee and Kantha (1989) applied in Flocco et al. (2024), rely primarily on two-dimensional idealizations, neglecting critical three-dimensional effects like flow splitting and blocking around an obstacle (Nikurashin et al., 2014) and keel sheltering (Wang et al., 2025). Because of the substantial number of parameters involved in characterizing this problem, previous numerical works were only able to consider a limited set and value ranges of parameters (e.g., Zu et al., 2021; Zhang et al., 2022; De Abreu et al., 2024; Wang et al., 2025). Therefore, a key goal of this study is to determine valid parameter ranges and relevant nondimensional parameters to efficiently constrain this space, guiding targeted numerical simulations and laboratory experiments required to improve existing parameterizations.

Our study applies Gaussian Mixture Modeling (GMM) to nondimensional parameters constructed from physical variables of the characteristics of the ice keels and the underlying ocean in the Arctic, aiming to identify mechanically distinct regions that influence ice—ocean interactions. GMM has previously been successfully used in oceanographic problems involving complex, spatially variable processes. For example, Jones and Ito (2019) employed GMM to classify regions of the global ocean based on the balance between physical and biogeochemical components of the surface carbon budget. Their unsupervised classification revealed four spatially coherent carbon regimes, consistent with theoretical expectations about ocean circulation and biogeochemical processes, demonstrating GMM's utility in objectively uncovering latent oceanographic structures. More recently, Ye and Zhou (2025) applied GMM to global ocean temperature profiles, identifying 18 distinct thermal regimes that align with known water masses and circulation features, further illustrating the method's effectiveness in uncovering physically meaningful oceanographic patterns.

In this paper we present both the clustering analysis of the Arctic sea ice-related nondimensional parameters and idealized numerical simulations for different nondimensional parameter regimes based on the clustering results. It is organized as follows. In § 2, we describe the five nondimensional parameters that characterize ice keel-ocean interactions, the dataset that we use to calculate these nondimensional parameters, and the GMM clustering methodology. § 3 outlines the set-up for numerical simulations as well as the kinetic energy metrics used to compare across the simulations. In § 4.1, we discuss our results for the clusters based on time-averaged nondimensional parameter values, comparing across the different regimes guided by the numerical simulation results. Specifically, we find regions of the Arctic closer land boundaries to be within parameter regimes of less internal wave generation and kinetic energy dissipation due to ice keel effects, whereas regions of the center Arctic to be in the regimes in which the flow is more affected by the moving ice keels, with greater internal wave generation and turbulence. Then, in § 4.2, we describe the spatial-temporal variability of the five nondimensional parameters and the effect of this variability on the parameterized ice keel-induced internal wave drag  $C_{\rm IW}$ . Finally, in § 5, we summarize our findings, putting these results into the context of previous numerical studies and providing suggestions on future numerical work.

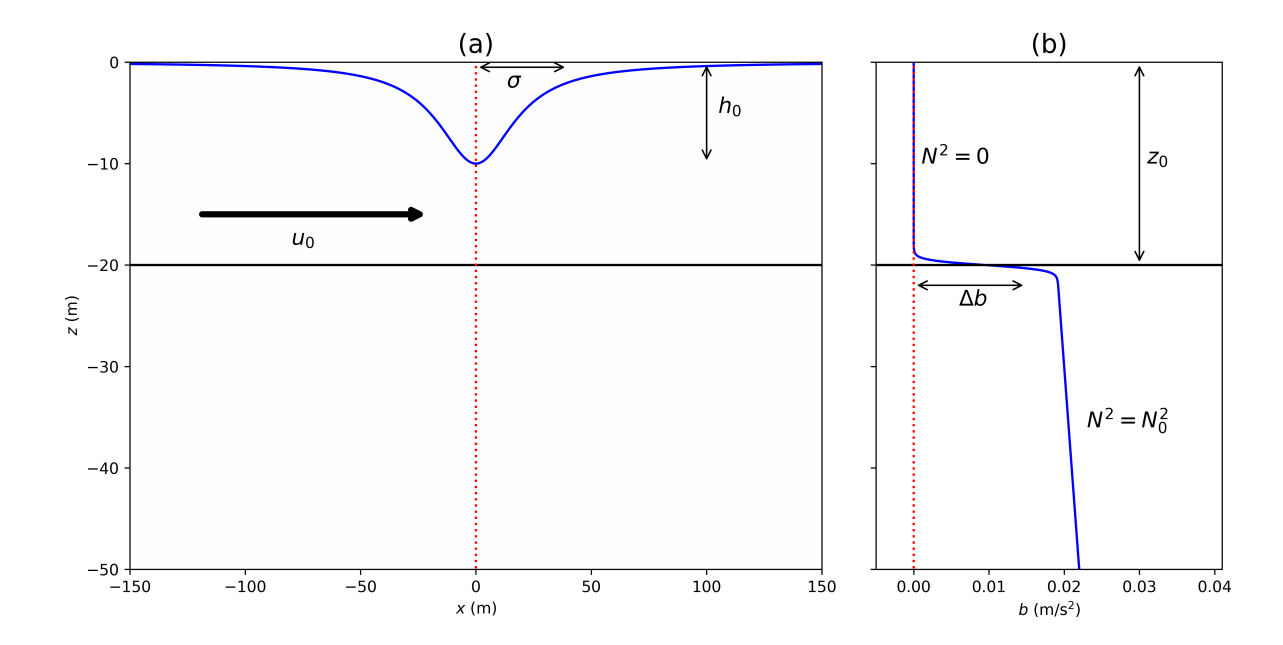


Figure 1. Schematic of sea ice keel moving relative to the the ocean with (a) dimensions (width  $\sigma$  and maximum depth  $h_0$ ) and speed of the ice keel relative to the ocean  $(u_0)$ , and (b) vertical stratification of the underlying ocean (mixed layer depth  $z_0$ , density jump across the pycnocline  $\Delta b$ , and buoyancy frequency below the pycnocline  $N_0$ ).

## 2 Data and GMM Methodology

95

100

105

We use output from Flocco et al. (2024) based on the ocean model NEMO (Nucleus for European Modelling of the Ocean) version 3.6 (Storkey et al., 2018) coupled with sea ice model CICE version 5.1 (Hunke et al., 2010). The model is atmospherically forced using NCEP-DOE-2 Reanalyses data (Kanamitsu et al., 2002) over the 2000 – 2017 time period. The details of model set-up, implementation, and validation are summarized in Flocco et al. (2024). The resulting dataset contains monthly-mean relevant sea ice and ocean variables over the 18 year period. The model output is, of course, merely an approximation of the real ocean sea ice state, limited by modeling assumptions, e.g., resolution and parameterization of small-scale processes. However, the goal of this study is to identify sea ice parameter regimes and parameter value ranges to ultimately improve sea ice drag parameterizations in ocean models. Therefore, it is adequate for this study to use an output from a sea ice-ocean coupled model as a representative sample.

When a drifting sea ice keel interacts with a stratified upper ocean, a number of dimensional variables determine how the system responds. Schematic view of the problem is shown in Figure 1. Keel geometry is set by its maximum depth  $h_0$  and horizontal spacing L. This definition of horizontal spacing follows previous theoretical works on flow induced by rough topography and sea ice (e.g., Bell Jr., 1975; McPhee and Kantha, 1989), where  $L = 2\pi/k_0$  for  $k_0$  being the horizontal wavenumber of a

sinusoidal topographic feature. Consistent with these theoretical works, we will limit this study to a two-dimensional model, with (x,z) representing horizontal and vertical directions, respectively. In more recent numerical studies (e.g., Skyllingstad et al., 2003; Zhang et al., 2022; De Abreu et al., 2024), it has been more common to model keel shape h(x) using a Versoria

$$h(x) = \frac{h_0 \sigma^2}{\sigma^2 + 4x^2},\tag{1}$$

with width  $\sigma$ , which we also use in our numerical simulations (see § 3). However, the CICEv5.1 model output reports L rather than  $\sigma$  and theoretical nondimensional numbers are typically expressed in terms of  $k_0$ , so we make the approximate connection that  $\sigma = \pi/(2k_0)$ .

The forcing arises from the horizontal velocity of the drifting ice relative the underlying ocean current, with components  $(u,v)=(u_{\rm ice}-u_{\rm ocean},v_{\rm ice}-v_{\rm ocean})$ . Combining the two velocity components, we define relative forcing magnitude to be  $u_0=\sqrt{u^2+v^2}$  (see Fig. 1(a)). The vertical stratification of the ocean is characterized as two layers: well-mixed layer of depth  $z_0$  with zero buoyancy frequency N=0 separated by a sharp pycnocline with buoyancy jump  $\Delta b$  from the lower weakly stratified layer with buoyancy frequency  $N_0$  (see Fig. 1(b)). Since these six dimensional quantities  $(u_0,h_0,k_0,z_0,\Delta b,$  and  $N_0)$  span different units and scales, it is more effective to describe the system in terms of nondimensional ratios that capture the relative importance of keel geometry, velocity forcing, and ocean stratification. These nondimensional parameters reduce the number of free variables and provide a compact framework to identify dynamical regimes.

The first one measures whether lee waves can radiate into the stratified interior (Nikurashin and Ferrari, 2010) and is defined as:

125 
$$\chi = \frac{u_0 k_0}{N_0}$$
. (2)

It represents the ratio of the wavenumber of the topography (keel)  $k_0$  to the wavenumber of radiating lee waves  $N_0/u_0$ . Theory predicts that freely-propagating lee waves are generated if  $0 < \chi < 1$ .

The second parameter compares the change in potential energy to move a parcel vertically over a distance of obstacle height in a stratified medium to the kinetic energy of the flow (Legg, 2021):

130 
$$J = \frac{N_0 h_0}{u_0}$$
. (3)

It can be also thought of as the ratio of obstacle height to the vertical wavenumber of the generated lee wave (Mayer and Fringer, 2017). When J is small (e.g., J < 1), the mean flow has enough kinetic energy to carry fluid parcels over the obstacle, such that lee waves are linear. When J is large (e.g., J > 1), linear theory becomes no longer valid and flow encountering the obstacle gets blocked, leading to nonlinear dynamics such as hydraulic jumps (Winters and Armi, 2012; Zemskova and Grisouard, 2022). Therefore, in theoretical studies of flow interaction with topographic obstacles, J is often a measure of nonlinearity of the flow dynamics.

The third parameter measures keel steepness:

110

115

120

function

$$\zeta = \frac{h_0}{L/2} = \frac{h_0 k_0}{\pi} = \frac{\chi J}{\pi}.\tag{4}$$

Greater  $\zeta$  corresponds steeper keel sides, i.e., to deeper and/or less wide keels.

The fourth parameter quantifies how far the keel protrudes below the mixed layer:

150

155

160

165

170

$$\eta = \frac{z_0}{h_0},\tag{5}$$

Smaller  $\eta$  indicates that the keel depth is comparable to  $(\eta \to 1)$  or exceeds the mixed layer depth  $(\eta < 1)$  and implies stronger mechanical coupling of the disturbance generated by the moving keel with the flow below the pycnocline.

The final parameter compares the potential energy barrier of the pycnocline to kinetic energy of the forcing:

145 
$$\operatorname{Ri} = \frac{\Delta b}{k_0 u_0^2}$$
, (6)

and is related to the Froude number Fr reported in previous studies (e.g., De Abreu et al., 2024) as:

$$Fr = \frac{1}{\sqrt{Ri}}.$$
 (7)

Smaller Ri (larger Fr) corresponds to a weaker pycnocline and/or stronger forcing and has been previously found to result in more unstable, supercritical flow conditions.

For each monthly time step and horizontal grid cell (at given latitude and longitude) in the NEMOv3.6 and CICEv5.1 model output from Flocco et al. (2024), we first compute the five nondimensional parameters using the corresponding sea ice and ocean variables. We then perform an initial filtering step to remove all samples (i.e., individual time–grid coordinate pairs) where the  $\chi$  falls outside the lee wave radiating range  $0 < \chi < 1$ . For each parameter, these filtered values are then averaged along the time dimension at every spatial grid point. This operation collapses the temporal variability into a single representative statistic, producing one time-averaged value per parameter for each horizontal grid cell across the model domain. To further reduce the influence of extreme values, for each parameter, we remove spatial grid points whose value exceeded the 95th percentile of that parameter's distribution, thereby reducing right-skewness and preventing a few extreme values from dominating the results. Filtering is applied in this way to predominantly exclude values with extremely large magnitudes. A grid cell was discarded if any of its parameter values fell outside its respective range. This two-stage filtering process produced a clean dataset of time-averaged nondimensional parameters as shown in Figure 2.

We then apply GMM to the set of nondimensional parameter values computed at each time step and horizontal grid location after filtering and time-averaging. GMM is an unsupervised clustering algorithm, similar to K-means, which separates data points into K clusters in M-dimensional space. Here, M=5 because we have five nondimensional variables. GMM was chosen because, unlike the K-means algorithm, it accommodates elliptical cluster shapes and provides probabilistic membership assignments, allowing for uncertainty quantification in cluster classification. The number of clusters K is not known a priori and has to be determined using the Bayesian Information Criterion (BIC) as shown in Figure 3. BIC score rewards higher probability of a data point belonging to one of the clusters, while punishing a large number of clusters. Therefore, one can run a parameter sweep selecting the configuration that minimized BIC across a tested range of the number of clusters K. In this paper, we choose K=6 because it is near the BIC curve's elbow point (Figure 3) and offers a good balance between model simplicity and interpretability, which diminishes with too many clusters (Jones and Ito, 2019). The GMM is fit to the

entire dataset of remaining parameter values (across all grid cells and time-averaged values), treating each observation as an independent sample in the five-dimensional parameter space. Cluster labels are then assigned to each observation based on the maximum posterior probability as shown in Figure 4, and the corresponding spatial patterns of these clusters are analyzed to interpret the underlying physical regimes.

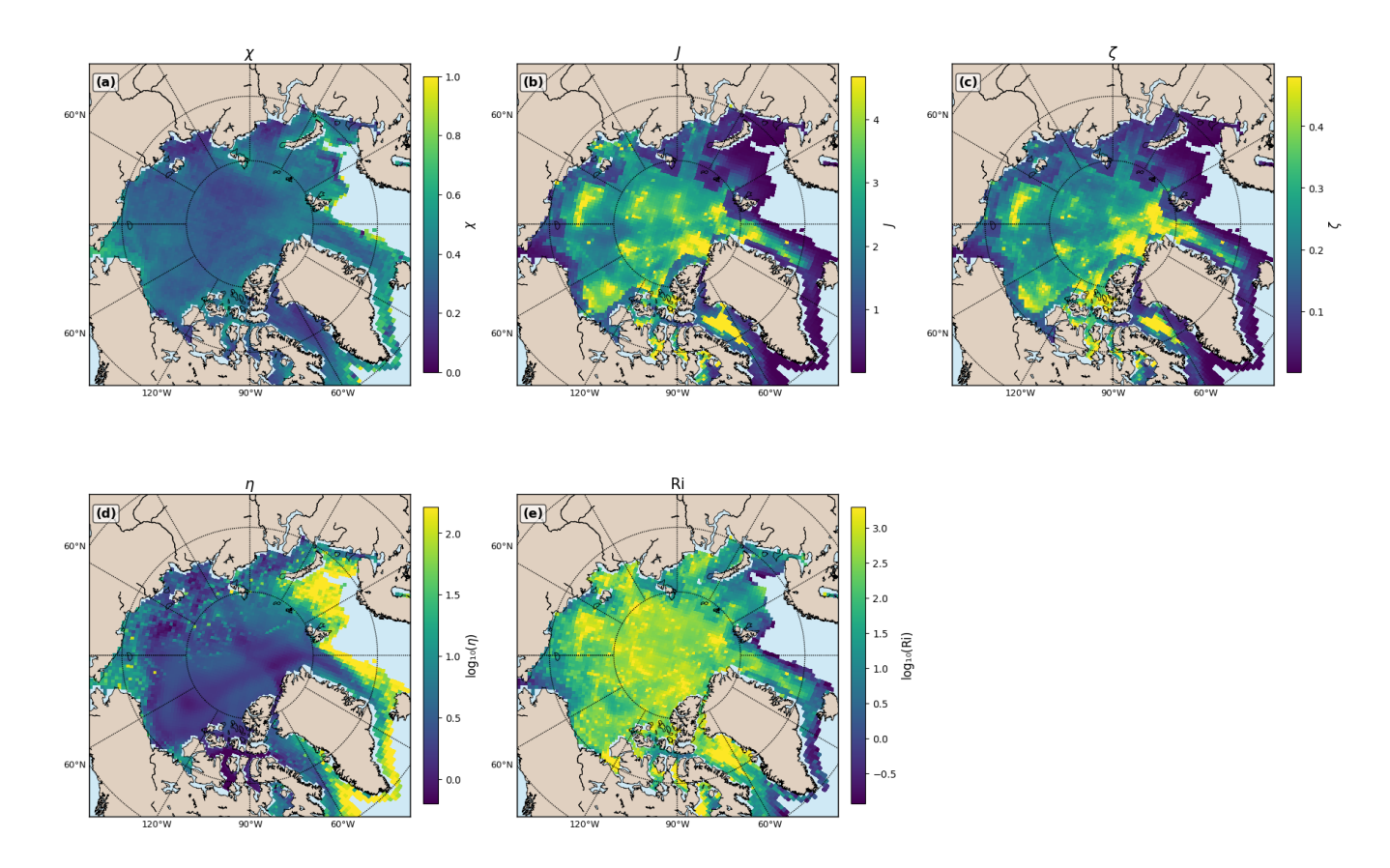


**Figure 2.** Spatial distribution of time-averaged five nondimensional variables over the Arctic Ocean: (a)  $\chi$ , (b) J, (c)  $\zeta$ , (d)  $\eta$ , and (e) Ri. All variables are defined in Eqns. (2)-(6). The post-processing of the variables is described in § 2. Note that colorbars vary across subplots and the magnitudes of (d)  $\eta$  and (e) Ri are shown on a logarithmic scale. Figure is made with Matplotlib Basemap toolkit library (https://matplotlib.org/basemap/stable/)

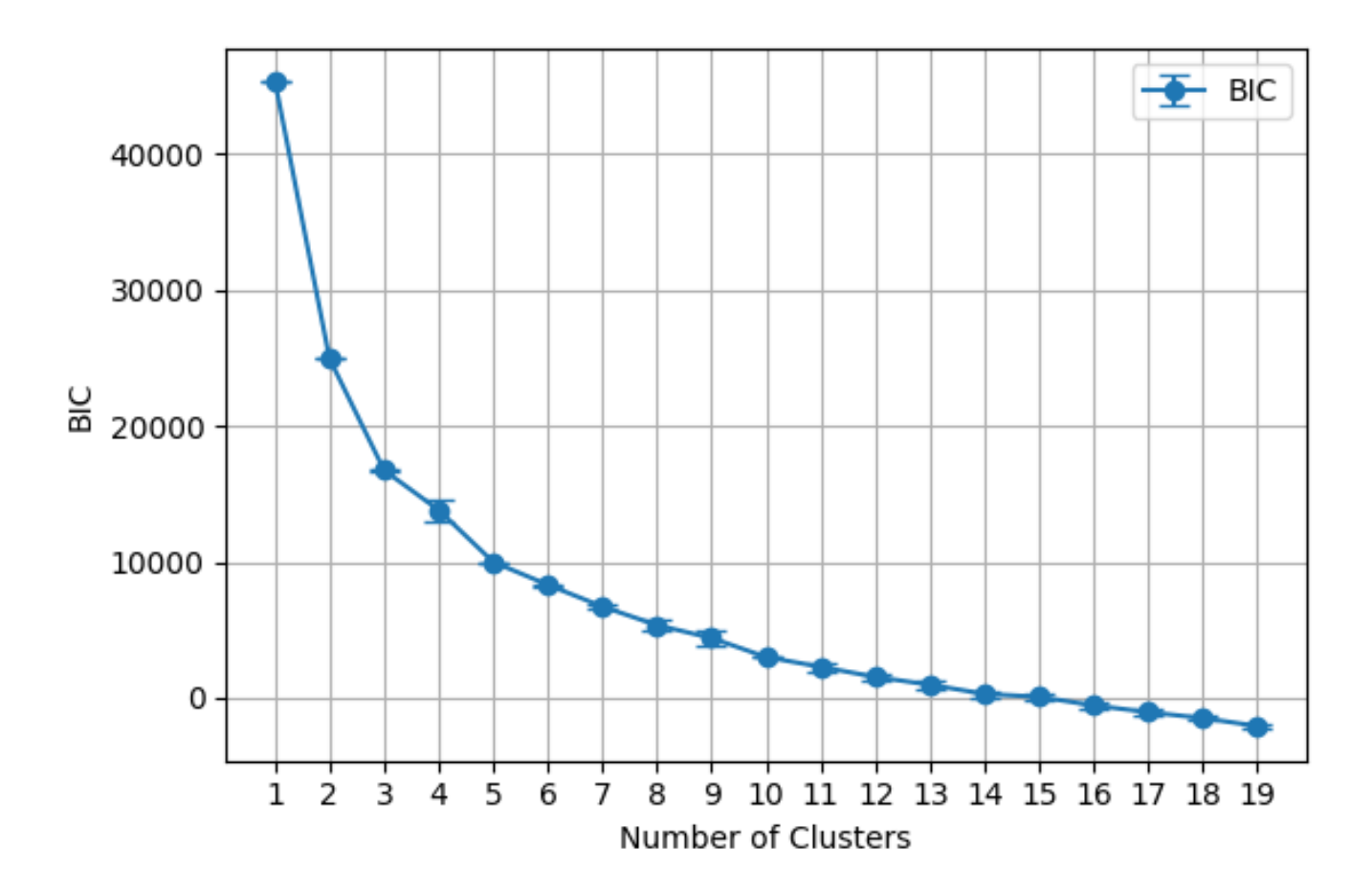
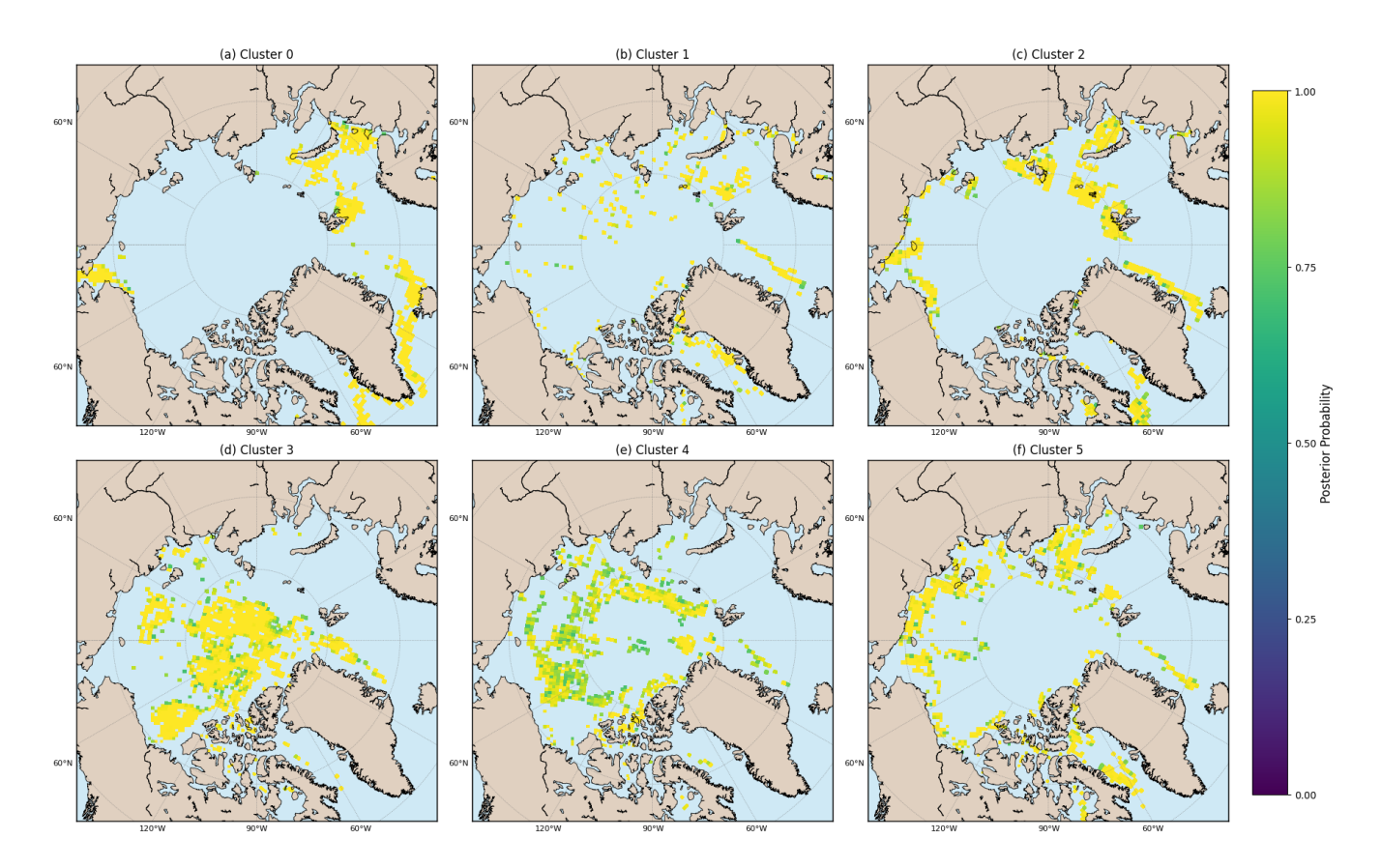


Figure 3. BIC scores for GMM fitted to the five-dimensional feature space composed of  $\chi$ , J,  $\zeta$ ,  $\eta$ , and Ri. Models were fitted for cluster numbers ranging from 1 to 19. Each model fitting was repeated 3 times with different random initializations to assess variability in BIC values; error bars indicate  $\pm 1$  standard deviation.

# 175 3 Numerical simulations

## 3.1 Set-up

In order to illustrate the differences in the dynamical regimes for each cluster identified by the GMM, we perform numerical simulations of the idealized problem shown in Figure 1. Similar to previous studies (e.g., Zhang et al., 2022; De Abreu et al., 2024), our simulations are two-dimensional in (x, z). Technically, the domain is two-and-a-half dimensional with just one grid cell in the y-direction, and the velocity in the y-direction can be non-zero but all derivatives with respect to y are zero.



**Figure 4.** Posterior probability maps for each of the six clusters identified by the GMM, based on time-averaged standardized nondimensional parameters  $(\chi, J, \zeta, \eta)$ , and Ri). Each subplot (a–f) shows the posterior confidence that a given spatial grid cell belongs to the respective cluster. Only points most likely assigned to that cluster are shown. Figure is made with Matplotlib Basemap toolkit library (https://matplotlib.org/basemap/stable/)

Specifically, we solve the following non-hydrostatic rotating Navier-Stokes equations with the Boussinesq approximation:

$$\frac{\partial \mathbf{u}}{\partial t} + \mathbf{u} \cdot \nabla \mathbf{u} - \mathbf{f} \times \mathbf{u} = -\frac{\nabla p}{\rho_0} + \nu \nabla^2 \mathbf{u} + b\mathbf{k} + f u_0 \mathbf{j}, \tag{8}$$

$$\frac{\partial b}{\partial t} + \mathbf{u} \cdot \nabla b = \kappa \nabla^2 b,\tag{9}$$

$$\nabla \cdot \mathbf{u} = 0,\tag{10}$$

where  $\mathbf{u} = (u, v, w)$  is the velocity in (x, y, z) directions, p is pressure,  $b = -g(\rho - \rho_0)/\rho_0$  is buoyancy for density  $\rho(x, z, t)$  and constant reference density  $\rho_0$ ,  $\mathbf{f} = f\mathbf{j}$  for local Coriolis parameter f,  $\mathbf{j}$  and  $\mathbf{k}$  are unit vectors in y and z directions, respectively, and  $\nu$  and  $\kappa$  are kinematic viscosity and diffusivity, respectively. For steady velocity forcing, the term  $fu_0$  is added to the y-momentum equation analogous to the simulations by Klymak (2018) and Zemskova and Grisouard (2021).

The equations are solved using *Oceananigans.jl* (Ramadhan et al., 2020; Wagner et al., 2025) to take advantage of the enhanced computational speeds by GPUs (Silvestri et al., 2025). In its current implementation, an immersed boundary grid to model an obstacle (e.g., bottom topography or an ice keel) can only be specified along the bottom boundary. However, we can apply the property of the Boussinesq flows in that the flow is symmetric when flipped vertically, assuming that the buoyancy is also flipped in sign. That is, for example, in the Boussinesq approximation, cool dense water sinking and warm light water rising appear as vertically-flipped mirror images. Therefore, we model a flipped version of Figure 1 by imposing a Versoria-shaped (Eqn. 1) immersed boundary along the bottom of the domain and initializing the buoyancy profile as

$$b_0(z) = \frac{1}{2} \left( \Delta b - N_0^2 \left( -H - z_0 - z \right) \right) \left( 1 - \tanh \left( \frac{-H - z_0 - z}{\mu} \right) \right), \tag{11}$$

where H is the maximum depth of the domain and  $\mu$  is the pycnocline width taken to be 0.5 m for all simulations. In order to avoid reflections off the top rigid-lid surface, we implement an exponential sponge layer  $e^{-z^2/2\delta^2}$  with  $\delta=-H/20$ , which corresponds to the sponge layer being applied within approximately the top 20 m. Within the sponge layer, the flow is relaxed with a damping rate of  $1/(20\Delta t)$  to the initial conditions:  $b_0(z)$  for buoyancy,  $u_0$  for u, and zero for w. In order to maintain numerical stability of the simulations, we take values for  $\nu$ ,  $\kappa$ , and  $\Delta t$  similar to those of De Abreu et al. (2024), namely,  $\nu=\kappa=10^{-3}$  m²/s and  $\Delta t=6\times 10^{-3}$  s. However, unlike De Abreu et al. (2024), we do not apply sponge layers along the left and right boundaries, as these sponge layers were found to trigger artificial disturbances that travel downstream generating flow instabilities. Instead, we set the horizontal boundaries to be periodic and run the simulations for 6 hours, which we found to be enough time for the flow to reach a quasi-steady state, but not enough time for the instabilities re-entering the domain through the periodic boundaries to reach the topographic obstacle. Finally, we set  $f=1.36\times 10^{-4}$  s<sup>-1</sup> corresponding to  $70^{\circ}$  N, though rotation is likely to not significantly influence the simulations as the total length of the simulation time is less than one inertial period ( $\approx 12.8$  hours).

The domain for all numerical simulations is  $x \in [-L_x/2, L_x/2]$  for  $L_x = 1200$  m and  $z \in [-H, 0]$  for H = 350 m. The only exception is Cluster 1, for which H = 500 m to account for a deeper pycnocline ( $\eta = 27, z_0 = 280$  m). For all simulations, we set  $u_0 = 0.1$  m/s and width of the Versoria-shaped obstacle (i.e., ice keel) as in Eqn. (1) to be  $\sigma = 40$  m. Recall that  $k_0 = \pi/2\sigma$ , We then compute all other dimensional parameters using the nondimensional parameter values as:

$$N_0 = \frac{u_0 k_0}{\chi}, \quad \Delta b = \text{Ri}k_0 u_0^2, \quad h_0 = \frac{\pi \zeta}{k_0}, \quad \text{and} \quad z_0 = -\eta h_0.$$
 (12)

We perform six numerical simulations taking the mean nondimensional parameter values  $\chi$ ,  $\zeta$ ,  $\eta$ , and Ri for each of the GMM clusters. These values are summarized in Table 1 and are further discussed in § 4. The horizontal resolution is the same for all simulations ( $N_x = 4096$  grid points), but the vertical resolution varies to allow approximately the same number of points within keel height  $h_0$ . As such, Cluster 0 simulation was discretized with  $N_z = 4096$  points, Clusters 1-2 simulation with  $N_z = 2048$  points, and Clusters 3-5 simulations with  $N_z = 1024$  points.

#### 3.2 Analysis metrics

200

205

To minimize the influence of the flow re-entering through periodic boundary conditions on the interpretation of our results, we limit the horizontal extent of the region of analysis for numerical simulations to  $x \in [-200, 200]$  m. All horizontal averages

**Table 1.** Mean and standard deviation (in parenthesis) values of each of the five nondimensional parameters for each of the six GMM clusters and the percent geographic area of the study domain that each cluster covers. All variables are defined in Eqns. (2)-(6). These values are based on the climatological mean values of each nondimensional variable. The mean values are also the ones used in numerical simulations described in § 3.

Cluster number	χ	ζ	J	η	Ri	% area
0	0.52	0.033	0.21	55	3.6	13
	(0.13)	(0.025)	(0.16)	(44)	(4.0)	
1	0.30	0.13	1.4	27	470	8.6
	(0.10)	(0.089)	(1.1)	(33)	(500)	
2	0.41	0.093	0.71	8.4	29	15
	(0.078)	(0.032)	(0.20)	(6.5)	(27)	
3	0.29	0.31	3.3	2.0	500	26
	(0.051)	(0.078)	(0.51)	(0.67)	(350)	
4	0.33	0.25	2.4	2.6	290	21
	(0.066)	(0.060)	(0.34)	(1.3)	(200)	
5	0.33	0.17	1.6	5.1	130	17
	(0.087)	(0.065)	(0.43)	(3.9)	(100)	

and integrals are performed only within these bounds. Also, in order to be consistent with the orientation of ice keel being at the surface (rather than along the bottom as in the numerical simulation set-up), all of the subsequent equations and figures will be shown in terms of  $\hat{z} = -H - z$ .

In order to compare the flow dynamics across the numerical simulations with different parameter regimes, we compute the turbulent kinetic energy

$$E_K(x,\hat{z}) = \frac{1}{2} \left( u'(x,\hat{z})^2 + w(x,\hat{z})^2 \right)$$
(13)

and turbulent kinetic energy dissipation

$$\epsilon_K(x,\hat{z}) = \nu \left( \left( \frac{\partial u'}{\partial x} \right)^2 + \left( \frac{\partial u'}{\partial \hat{z}} \right)^2 + \left( \frac{\partial w}{\partial x} \right)^2 + \left( \frac{\partial w}{\partial \hat{z}} \right)^2 \right), \tag{14}$$

where  $u'(x,\hat{z}) = u(x,\hat{z}) - u_0$  is the velocity of fluctuations defined as the deviation of horizontal velocity u from the background  $u_0$ .

We then compute the area-averaged integrals of  $E_K$  and  $\epsilon_K$  in three different vertical regions to understand the effects of the different parameter regimes on the flow. The first region denoted by subscript pyc is around the pycnocline, which we define to be  $z_0 \pm 10$  m, and the integral is notationally expressed as

235 
$$\langle \cdot \rangle_{pyc} = \frac{1}{A_{pyc}} \int_{-200}^{200} \int_{z_0 - 10}^{z_0 + 10} \cdot d\hat{z} dx.$$
 (15)

The second region denoted by subscript above is above the pycnocline, that is between the pycnocline and the ice keel, i.e.,

$$\langle \cdot \rangle_{above} = \frac{1}{A_{above}} \int_{-200}^{200} \int_{z_0 + 10}^{-h_0/3} \cdot d\hat{z} \, dx.$$
 (16)

The upper bound is taken to be  $\hat{z} = -h_0/3$  to exclude numerical boundary layer effects due to the immersed grid. The third region denoted by subscript below is below the pycnocline, i.e.,

240 
$$\langle \cdot \rangle_{below} = \frac{1}{A_{below}} \int_{-200}^{200} \int_{-H+50}^{z_0-10} \cdot d\hat{z} dx.$$
 (17)

The lower bound is taken to be  $\hat{z} = -H + 50$  m to exclude the sponge layer. In Eqns. (15)-(17),  $A_{pyc}$ ,  $A_{above}$ , and  $A_{below}$  are areas of each respective region. We report values that are time-averaged over the last hour of the simulation to account for any small-scale temporal fluctuations.

We expect that most of the influence of the ice keel on the flow will be confined within the mixed layer, i.e., above the pycnocline. As we aim to quantify the relative influence on the ice keel on the pycnocline and the stratified interior of the ocean below the pycnocline, for each simulation we also compute the ratios:

$$\frac{\langle E_K \rangle_{above}}{\langle E_K \rangle_{below}}, \qquad \frac{\langle \epsilon_K \rangle_{above}}{\langle \epsilon_K \rangle_{below}}, \qquad \frac{\langle E_K \rangle_{above}}{\langle E_K \rangle_{pyc}}, \qquad \frac{\langle \epsilon_K \rangle_{above}}{\langle \epsilon_K \rangle_{pyc}}. \tag{18}$$

The smaller magnitudes of these ratios indicate greater effects of the keel on the energy propagation and dissipation within the pycnocline region and below the pycnocline.

250 Finally, to measure the effects of the keel on stratification, we compute

$$\frac{N_{max}}{N_0}, \qquad \frac{N_{max}}{N_{muc}}, \tag{19}$$

where  $N_{max}$  is the maximum value of the buoyancy frequency at the end of the simulation period, and  $N_{pyc}$  and  $N_0$  are buoyancy frequency values of the pycnocline and the stratified interior layer for the initial conditions. The first ratio in Eqn. (19) measures the maximum change in stratification in the stratified interior below the pycnocline due to the entrainment of fluid from the pycnocline region. Larger values of this ratio indicate greater increase in stratification below the pycnocline due to the flow perturbations induced by the ice keel. The second ratio measures the reduction in the pycnocline strength, which larger values indicating greater smoothing of the density barrier between the mixed layer and the stratified interior.

## 4 Results

255

## 4.1 Cluster parameter regimes

Figure 5 shows six clusters within the Arctic region identified by applying GMM to five time-averaged nondimensional parameters. Each cluster reflects different oceanographic and sea ice conditions as will be discussed below. These clusters exhibit

**Table 2.** Area-averaged turbulent kinetic energy  $E_K$  and turbulent kinetic energy dissipation  $\epsilon_K$  averaged over the last hour of each numerical simulation. The regions of the simulation domain (within the pycnocline pyc, above the pycnocline above, and below the pycnoline below) are defined in Eqns. (15)-(17). The units for  $\langle E_K \rangle$  terms are  $m^2/s^2$  and for  $\langle \epsilon_K \rangle$  terms are  $m^2/s^3$ .

Cluster	$\langle E_K \rangle_{pyc} \left( 10^{-5} \right)$	$\langle E_K \rangle_{above} \left( 10^{-5} \right)$	$\langle E_K \rangle_{below} \left( 10^{-5} \right)$	$\langle \epsilon_K \rangle_{pyc} \left( 10^{-8} \right)$	$\langle \epsilon_K \rangle_{above} \left( 10^{-8} \right)$	$\langle \epsilon_K \rangle_{below} (10^{-8})$
0	$8.6 \times 10^{-3}$	0.20	$1.9 \times 10^{-3}$	$1.1 \times 10^{-4}$	0.79	$2.9 \times 10^{-5}$
1	$5.6 \times 10^{-3}$	2.5	$4.6 \times 10^{-6}$	$2.9 \times 10^{-3}$	0.39	$1.7 \times 10^{-7}$
2	1.2	4.9	0.15	0.11	2.0	$3.3 \times 10^{-3}$
3	28	350	0.28	30	87	$2.6 \times 10^{-2}$
4	23	210	0.29	18	33	$1.4 \times 10^{-2}$
5	5.4	43	0.18	1.8	4.5	$7.0 \times 10^{-3}$

coherent geographic patterns despite latitude and longitude not being used as input variables for the clustering. Geographically, Clusters 0, 1, and 2 predominantly occupy boundary regions, marking coastal zones and peripheral seas. They appear along energetic margins of Baffin Bay, the Greenland Sea, and the Barents Sea, where strong boundary currents and variable stratification are common (Huang et al., 2024; Korablev et al., 2014; Kolås et al., 2024). In contrast, Clusters 3, 4, and 5 emerge progressively outward from the central Arctic in more open ocean waters, demonstrating spatial gradients or transitions. Cluster 3 concentrates in the central Arctic basin, and Clusters 4-5 extend across the Chukchi, East Siberian, Laptev, and Kara Seas. This geographic pattern is significant, indicating that certain parts of the Arctic are consistently characterized by distinct combinations of nondimensional parameters as shown in Figure 6. In this subsection, we will focus on the mean values of the nondimensional parameters for each cluster (Table 1) and discuss the dynamics of the different parameter regimes supported by the numerical simulations results. Snapshots of the flow fields for the numerical simulations are shown in Figures 7-8 and the energetics metrics are summarized in Tables 2-3.

265

270

280

Clusters 0, 1, and 2 tend to represent boundary or transitional regimes with more extreme or distinctive parameter values. For example, Clusters 0 and 2 exhibit relatively small Ri values, while Cluster 1 shows the highest Ri of all clusters, suggesting very different stratification—shear balances across these regimes. In contrast,  $\eta$  is consistently higher in Clusters 0-2 than in Clusters 3-5, which may reflect enhanced mixing layer depth or reduced keel depth near boundaries. Notably, Cluster 0 exhibits the highest internal wave generation potential (mean value  $\overline{\chi}=0.52$ ), exceeding the  $\chi=0.3$  threshold for efficient lee wave generation over topography proposed by Nikurashin and Ferrari (2010). In regimes of larger  $\chi$ , lee waves can interact with near-inertial motions, such that wave—wave interactions enhancing turbulence. However, relatively small J ( $\overline{J}=0.21$ ) suggests that fluid motions are predominantly nonturbulent. Large value of  $\eta$  ( $\overline{\eta}=55$ , which is the largest across all clusters) indicates that the keel height is too small to penetrate below the mixed layer, suggesting weak mechanical coupling with the pycnocline and potentially limiting the vertical reach of wave-induced mixing. In fact, we find that the ice keel has negligible effect on the flow for this parameter regime (Fig. 7(a-d)). Both  $E_K$  and  $E_K$  are smaller by  $E_K$  and of the near-inertial simulation for this cluster compared with the other clusters (Table 2), and it is predominantly confined to the near-

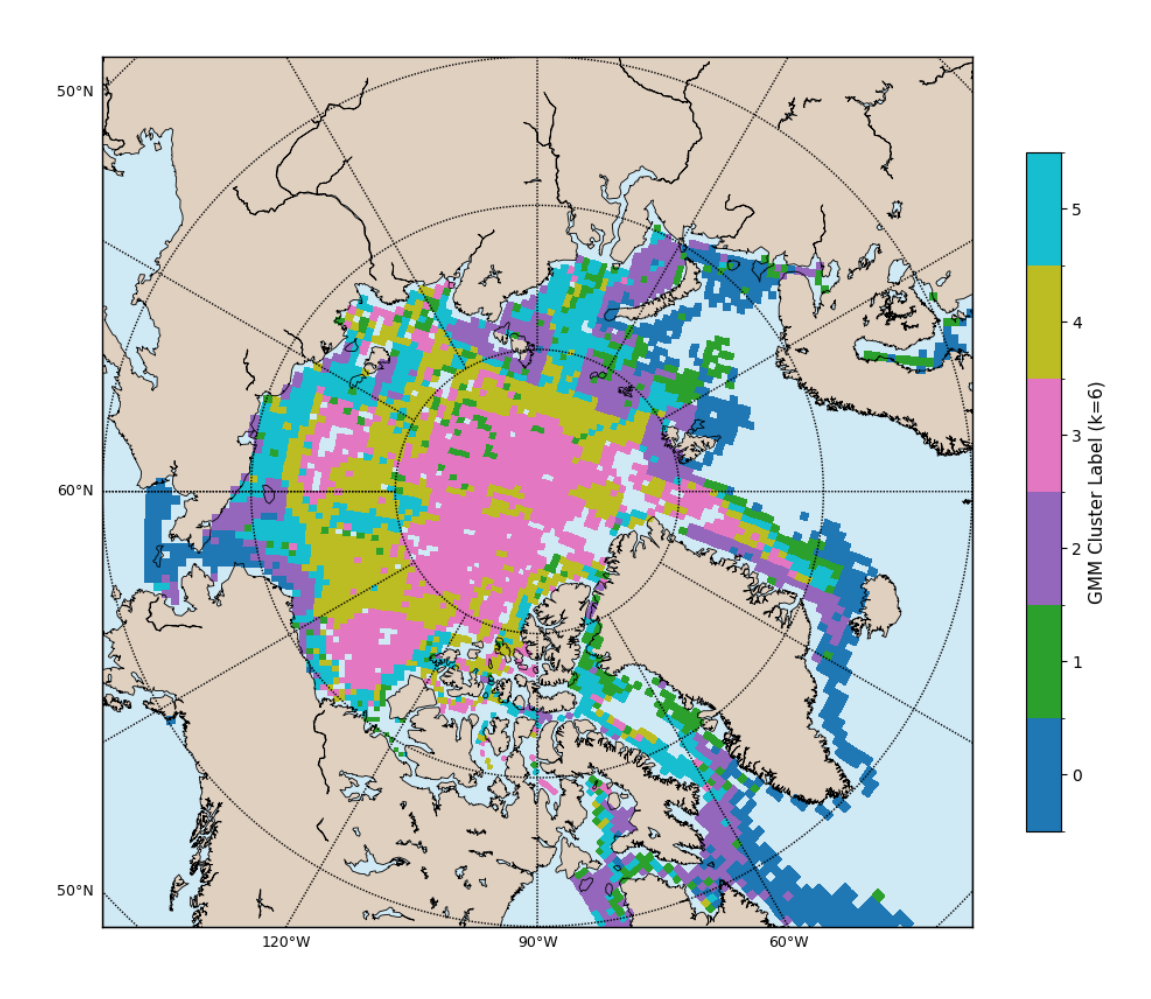
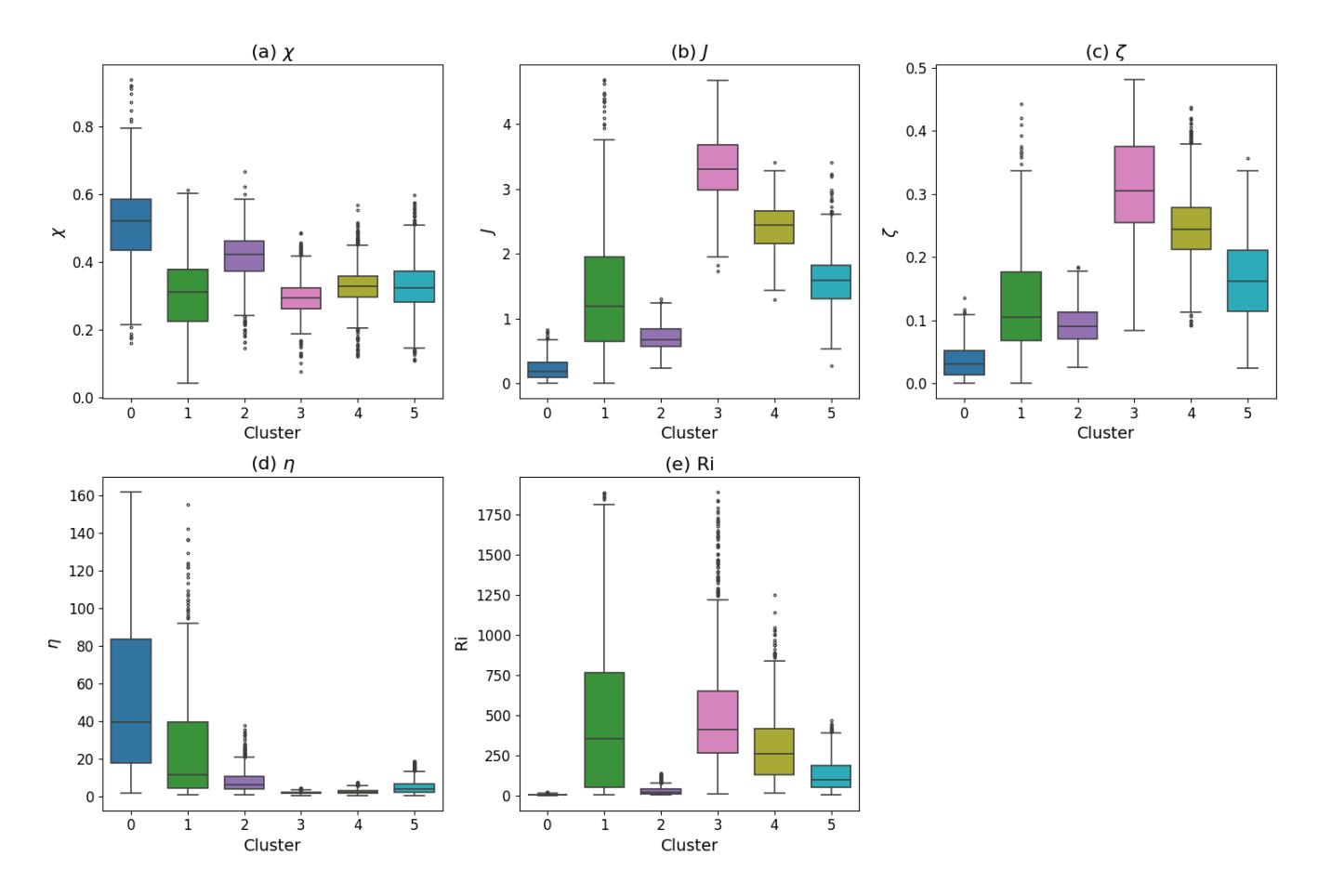


Figure 5. The spatial distribution of six statistically inferred regimes (K = 6), each represented by a unique color, over the Arctic Ocean domain, derived from a GMM fitted to standardized time-averaged nondimensional parameter values across all spatial grid points. Only grid cells with valid data for all five parameters were included in the analysis (see § 2) Figure is made with Matplotlib Basemap toolkit library (https://matplotlib.org/basemap/stable/).



**Figure 6.** Distribution of nondimensional variables across six GMM clusters based on annual-averaged nondimensional variable values shown in Fig. 5. Box plots summarize the spread of each computed nondimensional parameter ( $\chi$ , J,  $\zeta$ ,  $\eta$ , and Ri) across the six clusters identified by the GMM. Each subplot corresponds to a single parameter, with individual boxes showing the interquartile range, median, and outliers for each cluster.

keel region: both ratios of  $\langle E_K \rangle_{above} / \langle E_K \rangle_{below}$  and  $\langle \epsilon_K \rangle_{above} / \langle \epsilon_K \rangle_{below}$  are second largest across the simulations, only smaller than those of Cluster 1 (Table 3).

Cluster 1 is marked by a relatively large Richardson number ( $\overline{\rm Ri}=470$ ) and small keep depth and/or deep pycnocline ( $\overline{\eta}=27$ ), both likely to suppress turbulence. Despite flow likely being nonlinear and turbulent ( $\overline{J}=1.4$ ), the stable stratification likely inhibits wave breaking, as suggested by findings of De Abreu et al. (2024) that such environments tend to support only localized and intermittent dissipation. From the numerical simulations, we find most of the kinetic energy confined to the region above the pycnocline (Fig. 7(e-h), Table 3). While  $\langle E_K \rangle$  above the pycnocline is larger than that of Cluster 0 simulations, most likely due to a steeper keel ( $\overline{\zeta}=0.13$ ), both the kinetic energy magnitude and dissipation rates below the pycnocline are the

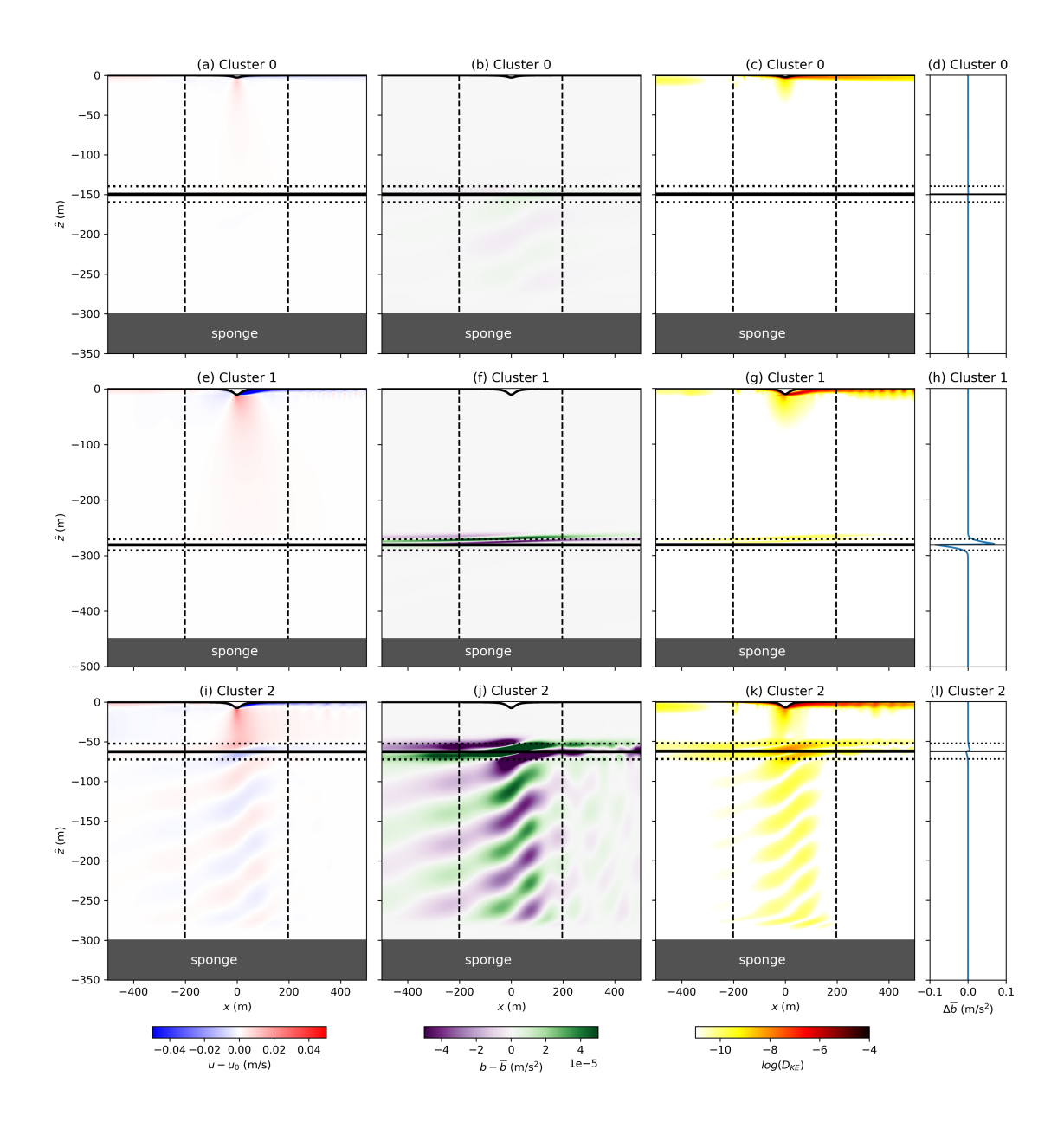
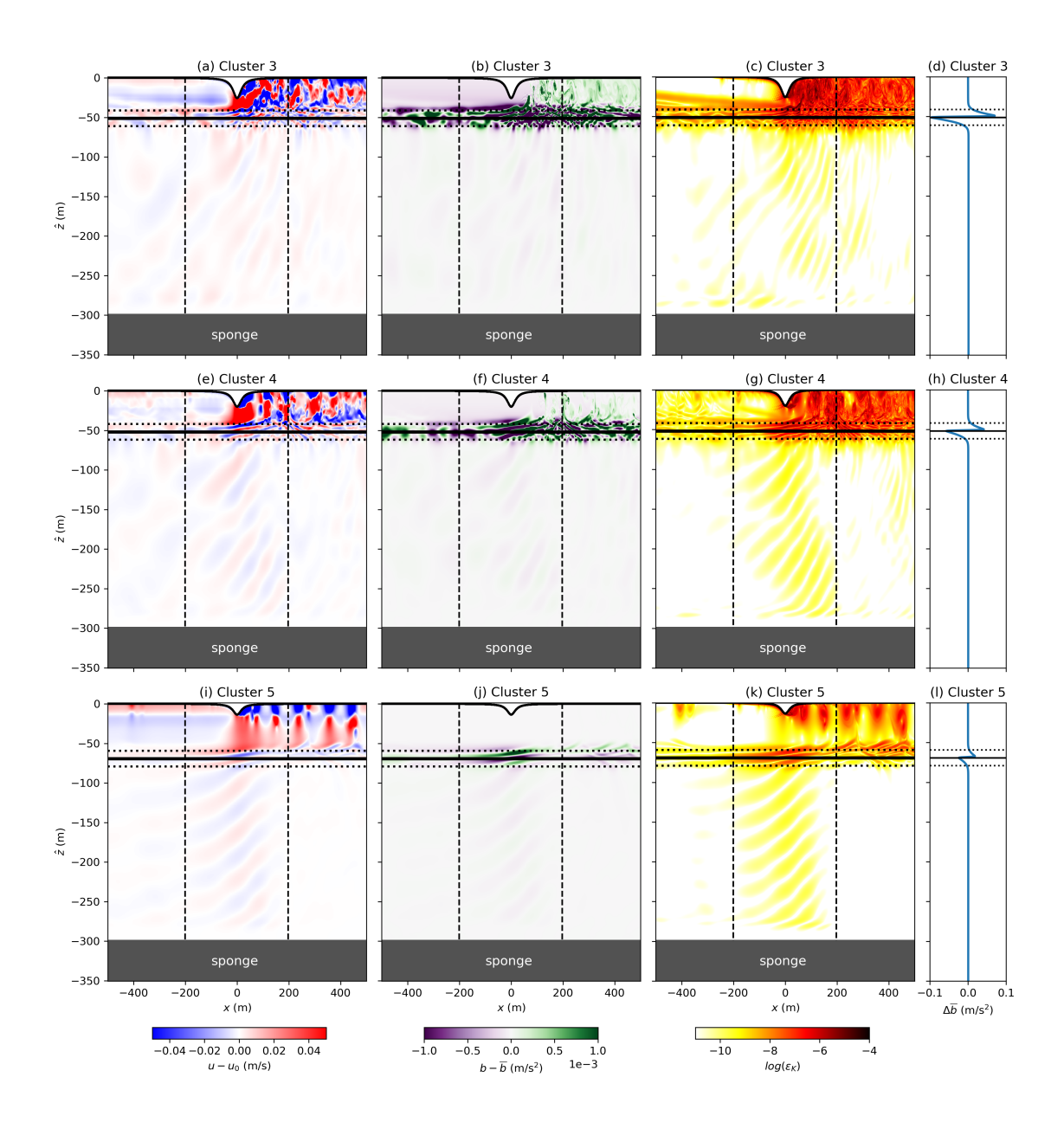


Figure 7. Snapshots from numerical simulations set with nondimensional parameters for GMM clusters 0 (a-d), 1 (e-h), and 2 (i-l): (a, e) turbulent horizontal velocity  $u-u_0$ , (b, f) buoyancy perturbations, i.e., deviations from horizontally-averaged  $\bar{b}(z)$ , (c, g) log of kinetic energy dissipation  $\epsilon_K$ , and (d, h) buoyancy deviation from initial conditions  $\Delta \bar{b} = \bar{b}(z) - b_0(z)$ . The thick black horizontal black lines in each subplot indicate the pycnocline  $\hat{z} = z_0$  and horizontal dotted lines delineate  $\hat{z} = z_0 \pm 10$  m. In (a-c, e-g), dashed vertical lines delineate the region  $x \in [-200, 200]$  m, which is used for horizontal averages and integrals. All snapshots are for the last timestep (after 6 hours) of simulation time.



**Figure 8.** Same as Figure 7 but for (a-d) Cluster 3, (e-h) Cluster 4, and (i-d) Cluster 5. Note that the colorbar in (b, f, j) for the buoyancy plots are different from those in Figure 7.

Table 3. Ratios of kinetic energy and stratification metrics to estimate the relative effects of the ice keel on the pycnocline and stratified interior below the pycnocline in each numerical simulation. Area-averaged turbulent kinetic energy  $E_K$  and turbulent kinetic energy dissipation  $\epsilon_K$  averaged over the last hour of each numerical simulation. The regions of the simulation domain (within the pycnocline pyc, above the pycnocline above, and below the pycnoline below) are defined in Eqns. (15)-(17).  $N_{max}$  is the maximum value of the buoyancy frequency at the end of the simulation period, whereas  $N_{pyc}$  and  $N_0$  are the buoyancy frequency at the pycnocline and within the stratified interior of the simulation initial condition.

Cluster	$\frac{\langle E_K \rangle_{above}}{\langle E_K \rangle_{below}}$	$\frac{\langle \epsilon_K \rangle_{above}}{\langle \epsilon_K \rangle_{below}}$	$\frac{\langle E_K \rangle_{above}}{\langle E_K \rangle_{pyc}}$	$\frac{\langle \epsilon_K \rangle_{above}}{\langle \epsilon_K \rangle_{pyc}}$	$\frac{N_{max}}{N_0}$	$\frac{N_{max}}{N_{pyc}}$
0	100	$2.7 \times 10^4$	23	$7.0 \times 10^{3}$	1.4	0.29
1	$5.5\times10^5$	$2.2 \times 10^{6}$	450	130	8.1	0.26
2	32	600	4.0	18	2.8	0.26
3	$1.2\times10^3$	$3.4 \times 10^{3}$	12	2.9	8.2	0.27
4	710	$2.3 \times 10^3$	9.0	1.9	7.1	0.27
5	230	650	7.9	2.5	4.7	0.27

smallest across all simulations (Table 2) as wave propagation is getting suppressed by the deep pycnocline and large buoyancy jump across the pycnocline.

295

300

305

Cluster 2 exhibits a blend of characteristics, with a moderately large value of  $\overline{\chi}=0.41$  suggesting potential wave-wave interactions, smaller value of  $\overline{J}=0.71$  suggesting relatively linear flow motions, and intermediate stratification strength ( $\overline{Ri}=29$ ) and keel depth ( $\overline{\eta}=8.4$ ), suggesting a regime in-between strongly forced and weakly stratified conditions. These conditions suggest occasional lee wave generation and intermittent mixing, likely governed by the interplay between moderate mechanical forcing and stratification. Indeed, we find lee waves radiating below the pycnocline in the numerical simulations for this regime (Fig. 7(i-1)). While  $E_K$  and  $\epsilon_K$  are smaller in magnitude in comparison with those for Clusters 3-5, kinetic energy around the pycnocline  $\langle E_K \rangle_{pyc}$  and below the pycnocline  $\langle E_K \rangle_{above}$  is relatively large (Table 2). The dissipation within the pycnocline region is relatively small (larger value of  $\langle \epsilon_K \rangle_{above} / \langle \epsilon_K \rangle_{pyc}$ ) suggesting more linear, less turbulent motions consistent with the dynamics expected from J<1 for less steep obstacles (Nikurashin and Ferrari, 2010; Zemskova and Grisouard, 2021). However, relatively smaller values of  $\langle \epsilon_K \rangle_{above} / \langle \epsilon_K \rangle_{below}$  suggest enhanced dissipation below the pycnocline, possibly due to the interaction between lee-waves and near-inertial waves described in Nikurashin and Ferrari (2010) and Zemskova and Grisouard (2021) for  $\chi>0.3$ .

Conversely, Clusters 3, 4, and 5, which encompass the more open-ocean areas, display systematic gradients in parameter values as we move from the center Arctic outward towards the marginal seas, suggesting evolving physical processes or spatial variations in ice-ocean coupling strength across broader Arctic regions from the open central Arctic toward the coastal regions. Cluster 3 is characterized by the largest mean value of wave nonlinear parameter ( $\overline{J} = 3.3$ ) and the largest value of keel steepness ( $\overline{\zeta} = 0.31$ ), indicating that keels in this region possess strong potential to overcome stratification and drive vertical mixing. In the numerical simulations, we find large turbulent velocities and dissipation rates, in particular above the pycnocline (Fig. 8(a,c)). The stratification in the vicinity of the pycnocline is also perturbed with evidence of small-scale

turbulent motions, and the deviation from the initial stratification  $\Delta \bar{b}$  is the largest across all simulations (Fig. 8(b,d)). However, the large Richardson number ( $\overline{\text{Ri}} = 500$ ) reflects strong density stratification, which may suppress sustained turbulence and limit mixing to localized, shear-driven interfaces. We find energy propagation below the pycnocline into the stratified interior to be small (large values of  $\langle E_K \rangle_{above} / \langle E_K \rangle_{below}$  and  $\langle \epsilon_K \rangle_{above} / \langle \epsilon_K \rangle_{below}$ ). This suggests that the large value of density jump across the pycnocline (large Ri) can inhibit the effect of the ice keel despite the small value of  $\overline{\eta} = 2.0$ , smallest across all clusters (so keel depth is largest relative to mixed layer depth). Furthermore, the relative small value of  $\overline{\chi} = 0.29$  suggests that the coupling between lee waves and near-inertial waves is weak, leading to relatively weaker dissipation rates below the pycnocline. This parameter pattern is consistent with the central-basin hydrography: a strong, salinity-controlled halocline characterizes these basins and tends to inhibit vertical exchange; thus, even where  $\chi$  and J are elevated and  $\eta$  is small (deeper, steeper keels), mixing is expected to be sporadic and shear-localized (Metzner and Salzmann, 2023).

Clusters 4-5 extend across the Chukchi, East Siberian, Laptev, and Kara Seas, where seasonal freshwater input and melt often produce strong summer stratification; thus uniformly "weak stratification" should not be assumed, and episodes of reduced Ri can arise where winds and shelf processes redistribute freshwater or enhance mixing (Carmack et al., 2016). Against this backdrop, Cluster 4 displays slightly smaller nonlinear parameter ( $\overline{J}=2.4$ ), keel steepness ( $\overline{\zeta}=0.25$ ), and pycnocline strength ( $\overline{Ri}=290$ ) than Cluster 3. Using the bulk scaling  ${\rm Fr}\sim{\rm Ri}^{-1/2}$  with consistent scales,  ${\rm Ri}=290$  implies a low Froude number  ${\rm Fr}\approx0.06$ . Based on the results of De Abreu et al. (2024), such low-Fr regimes tend to remain mixing-limited unless mechanical forcing (keel speed and draft) is strong and vortex shedding is active. From numerical simulations, the dynamics are similar to that of Cluster 3 simulations, but with slightly smaller  $E_K$  and  $\epsilon_K$  (Fig. 8(e,g)) due to smaller values of  $\zeta$  and J. The larger  $\overline{\eta}=2.6$  further indicates a deeper mixed layer relative to the keel draft, so the keel is less likely to contact or perturb the pycnocline (Fig. 8(f,h)) compared with Cluster 3. However, because of a smaller density jump across the pycnocline (smaller Ri), the lee-wave signature below the pycnocline is more coherent and the relative energy propagation below the pycnocline is larger (smaller values of  $\langle E_K \rangle_{above} / \langle E_K \rangle_{below}$  and  $\langle \epsilon_K \rangle_{above} / \langle \epsilon_K \rangle_{below}$ ) compared to Cluster 3.

Cluster 5 continues this trend moving away from the center Arctic towards the shelves with smaller  $\overline{J}=1.6$  and smaller  $\overline{\rm Ri}=130$ , pointing to a weaker pycnocline and greater susceptibility to intermittent internal-wave activity below the pycnocline. Its  $\overline{\chi}=0.33$  is around the wave-wave interaction threshold between near-inertial waves and lee waves, suggesting that in this weaker-stratification regime, wave-wave coupling can be an important driver of turbulence. The numerical simulations show overall smaller magnitude  $E_K$  and  $\epsilon_K$  and less turbulent motions around the pycnocline (Fig. 8(i-1)) compared to Cluster 3-4 simulations, most likely due to smaller J and  $\zeta$  (reduced nonlinearity of the flow) and larger  $\eta$  (small keel compared to mixed layer depth). However, because of smaller Ri, wave energy propagation into the stratified interior below the pycnocline is larger (smaller  $\langle E_K \rangle_{above} / \langle E_K \rangle_{below}$ ) in comparison to Clusters 3-4. Overall, as  $\overline{\eta}$  increases from  $\sim 2.0$  to  $\sim 5.1$  across Clusters 3-5, keels become progressively shallower relative to the mixed-layer depth, implying reduced mechanical coupling with the pycnocline, with the accompanying decreases in  $\overline{J}$  and  $\overline{\rm Ri}$  reflecting the shelf-sea pattern of a shallower pycnocline and enhanced shear from shelf-break currents (Carmack et al., 2016).

In general, we find that most of the energetics metrics (with the exception of  $N_{max}/N_{pyc}$  and  $\langle \epsilon_K \rangle_{above}/\langle \epsilon_K \rangle_{pyc}$ ) increase with increasing  $\zeta$ , Ri and J and decreasing  $\chi$  and  $\eta$ . It is particularly interesting to consider these trends for the ratios of these

metrics above and below the pycnocline:  $\langle \epsilon_K \rangle_{above} / \langle \epsilon_K \rangle_{below}$  and  $\langle E_K \rangle_{above} / \langle E_K \rangle_{below}$ . As  $\chi$  increases, there is greater coupling between generated near-inertial waves and lee waves (Nikurashin and Ferrari, 2010; Zemskova and Grisouard, 2021), so the internal wave effects at and below the pycnocline are stronger, leading to larger  $E_K$  and  $\epsilon_K$ , consistent with our findings. Larger Ri makes it more difficult for wave energy to penetrate below the pycnocline, thus increasing the relative magnitude of  $E_K$  and  $\epsilon_K$ , also consistent with our findings. However, as  $\zeta$  and J increase, one would expect more non-linear turbulent motions (Zemskova and Grisouard, 2021) and thus proportionally larger  $\langle E_K \rangle_{below}$  and  $\langle \epsilon_K \rangle_{below}$ , which is opposite to our findings. Similarly, as  $\eta$  decreases and the keel depth approaches that of the mixed layer depth, keel effect below the pycnocline would be expected to increases, thus increasing ratios of  $\langle \epsilon_K \rangle_{above} / \langle \epsilon_K \rangle_{below}$  and  $\langle E_K \rangle_{above} / \langle E_K \rangle_{below}$ . Yet, we find the opposite trend, suggesting that for these parameter value combinations, the effects of  $\chi$  and Ri are relatively more important compared to the effects of  $\eta$ ,  $\zeta$ , and J, with the exception of when  $\eta$  is too large such that there is almost no effect from the keel (e.g., Clusters 0-1).

#### 4.2 Variability of nondimensional parameters

While in the previous section we explored specific combinations of parameter values associated with each cluster, in this section, we consider the variability of the nondimensional parameters in order to identify the ranges of values that are relevant to the sea ice keels. Figure 9 shows the pair-wise distribution of nondimensional parameters  $\chi$ ,  $\zeta$ ,  $\eta$ , and Ri (J is omitted because the distribution is similar to  $\zeta$ ) calculated based on ice keel and ocean variables averaged annually, over the summer months (June-August), and over the winter months (December-February). One of the important results is the temporal variability of the ice keel-related nondimensional parameters. For instance, we find overall smaller values of  $\eta$  in the summer compared to the winter and annual averages, consistent with deeper ice keels predominantly found in colder months and shallower mixed layers in summer months (Fig. 9(b, d, f)). The larger  $\eta$  values in the annual averaged plot are possibly due to larger keel depths in April and May when the average sea ice thickness is at a maximum (Flocco et al., 2024). We also find overall  $\zeta$  limited to the range of smaller values, that is, less steep keels, in the winter months compared to the summer and annual averaged ranges (Fig. 9(c, d, e)). As the keel depth  $h_0$  is likely larger in the winter (also consistent with larger  $\eta$  in winter months), this implies that ice keel horizontal wavenumber  $k_0$  is smaller, that is the horizontal width is larger, in the winter compared to summer months. Interestingly, the ranges of values for  $\chi$  and Ri are approximately consistent throughout the year (Fig. 9(c)), pointing to relatively similar ranges and combinations of  $u_0$  and  $\Delta b$  values.

The second important result from Figure 9 is the relevant value ranges for each nondimensional variable and also the joint distributions of values. Ultimately, we wish to perform numerical simulations with parameter sweeps over these nondimensional parameters to test parameterization schemes included in regional and large-scale models, so it is important to limit the range of values for such sweeps. From Figure 9, we find that full combination of  $\chi - \eta$ ,  $\chi - Ri$ , and  $\zeta - Ri$  value ranges might need to be explored. On the other hand, there are certain parameter value combinations that we do not find relevant to ice keels, for example: large  $\chi$  and large  $\zeta$ , large  $\chi$  and large Ri, large  $\zeta$  and large  $\eta$ , and large Ri. This finding can help limit the number of numerical simulations that need to be conducted.

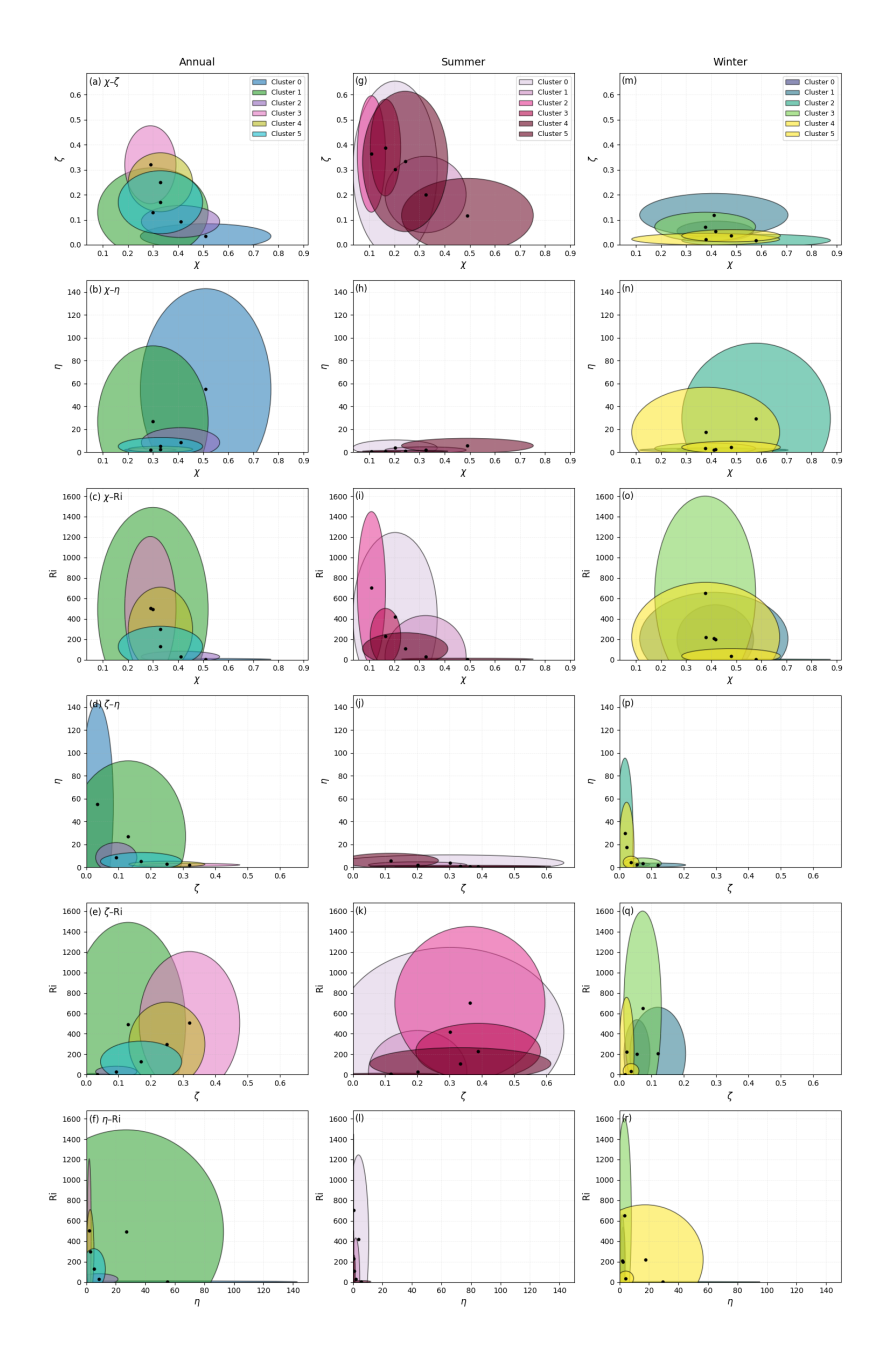


**Figure 9.** Pairwise ellipse plots showing the cluster-mean values and associated variability across six GMM-identified regimes (columns: Annual, Summer, Winter). Each colored ellipse is centered at the cluster mean for the variable pair shown and spans two standard deviations along each axis, capturing the internal spread of that cluster. Subplot labels (a)–(f) correspond to the following pairs: (a)  $\chi$ – $\zeta$ , (b)  $\chi$ – $\eta$ , (c)  $\chi$ –Ri, (d)  $\zeta$ – $\eta$ , (e)  $\zeta$ –Ri, and (f)  $\eta$ –Ri. Summer values are calculated over June–August; winter values are calculated over December–February.

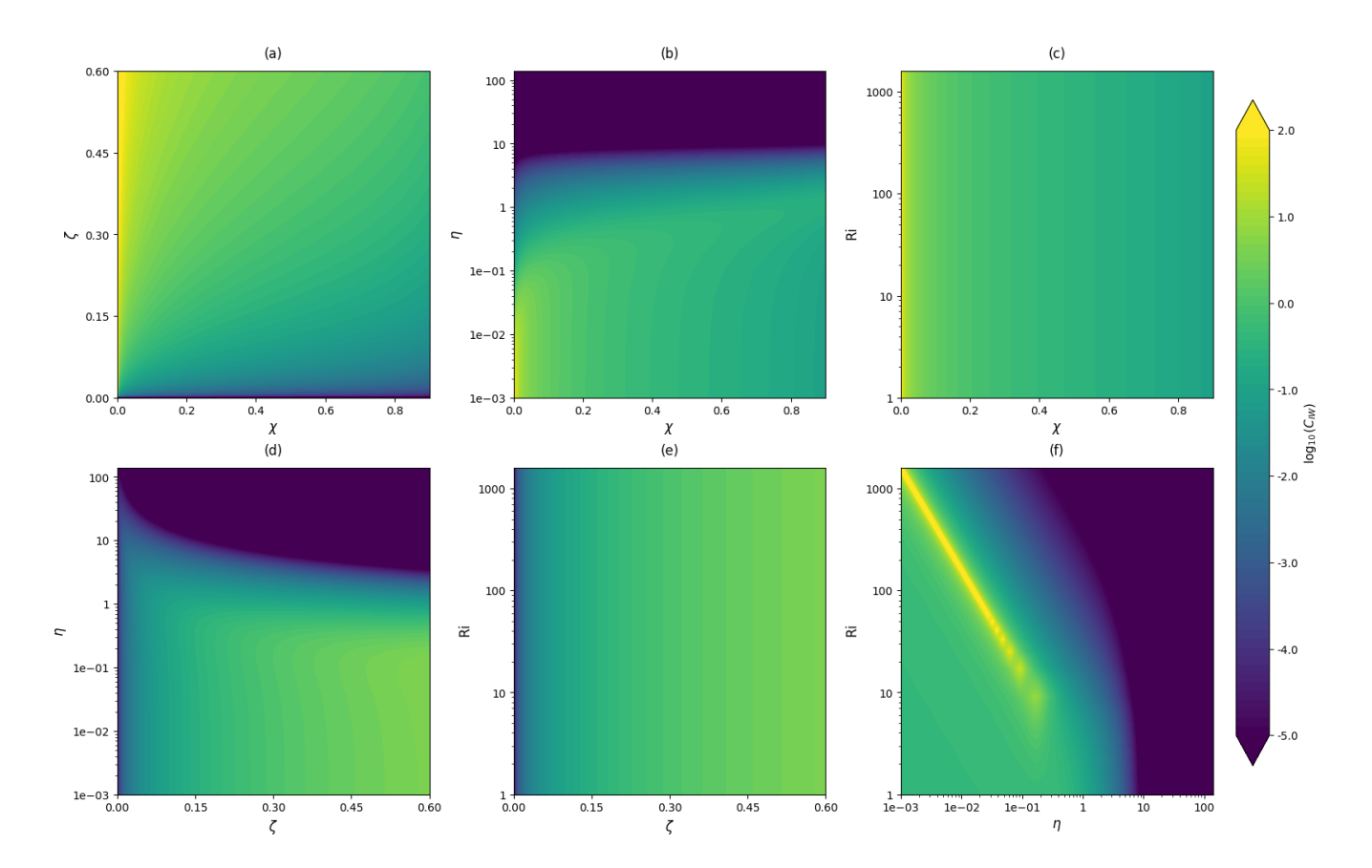


Figure 10. Contour plots of the internal wave drag coefficient  $\log(C_{\rm IW})$  as a function of pairwise combinations of the nondimensional parameters  $\chi$ ,  $\zeta$ ,  $\eta$ , and Ri, evaluated using equations from Flocco et al. (2024). In each subplot, one pair of variables is varied over a regular grid, while the remaining two parameters are held fixed at typical values ( $\chi = 0.4$ ,  $\zeta = 0.2$ ,  $\eta = 0$ , Ri = 1.0). The contours show how  $C_{IW}$  varies across each 2D parameter space. Logarithmic scaling is applied to  $\eta$  and Ri axes to capture its wide dynamic range. Subplot labels (a)–(f) correspond to the following parameter pairs: (a)  $\chi$ – $\zeta$ , (b)  $\chi$ – $\eta$ , (c)  $\chi$ –Ri, (d)  $\zeta$ – $\eta$ , (e)  $\zeta$ –Ri, and (f)  $\eta$ –Ri.

One of the currently parameterized quantity is the internal wave drag coefficient induced by moving ice keels,  $C_{\rm IW}$ , which provides a metric to quantify how sea ice interacts with and impacts the stratified upper ocean. Following McPhee and Kantha (1989),  $C_{\rm IW}$  is expressed as the product of a drag coefficient for a fully stratified water column,  $C_{\rm DNW}$ , and a damping factor  $\Gamma$  that depends on the buoyancy jump and mixed layer depth:

385

$$C_{\rm IW} = \Gamma C_{\rm DNW}. \tag{20}$$

The damping factor  $\Gamma$  accounts for the reduction of drag due to finite mixed-layer depth. The formulations for  $C_{\rm DNW}$  and  $\Gamma$  given in McPhee and Kantha (1989) and Flocco et al. (2024) are written in terms of dimensional sea ice- and ocean-related

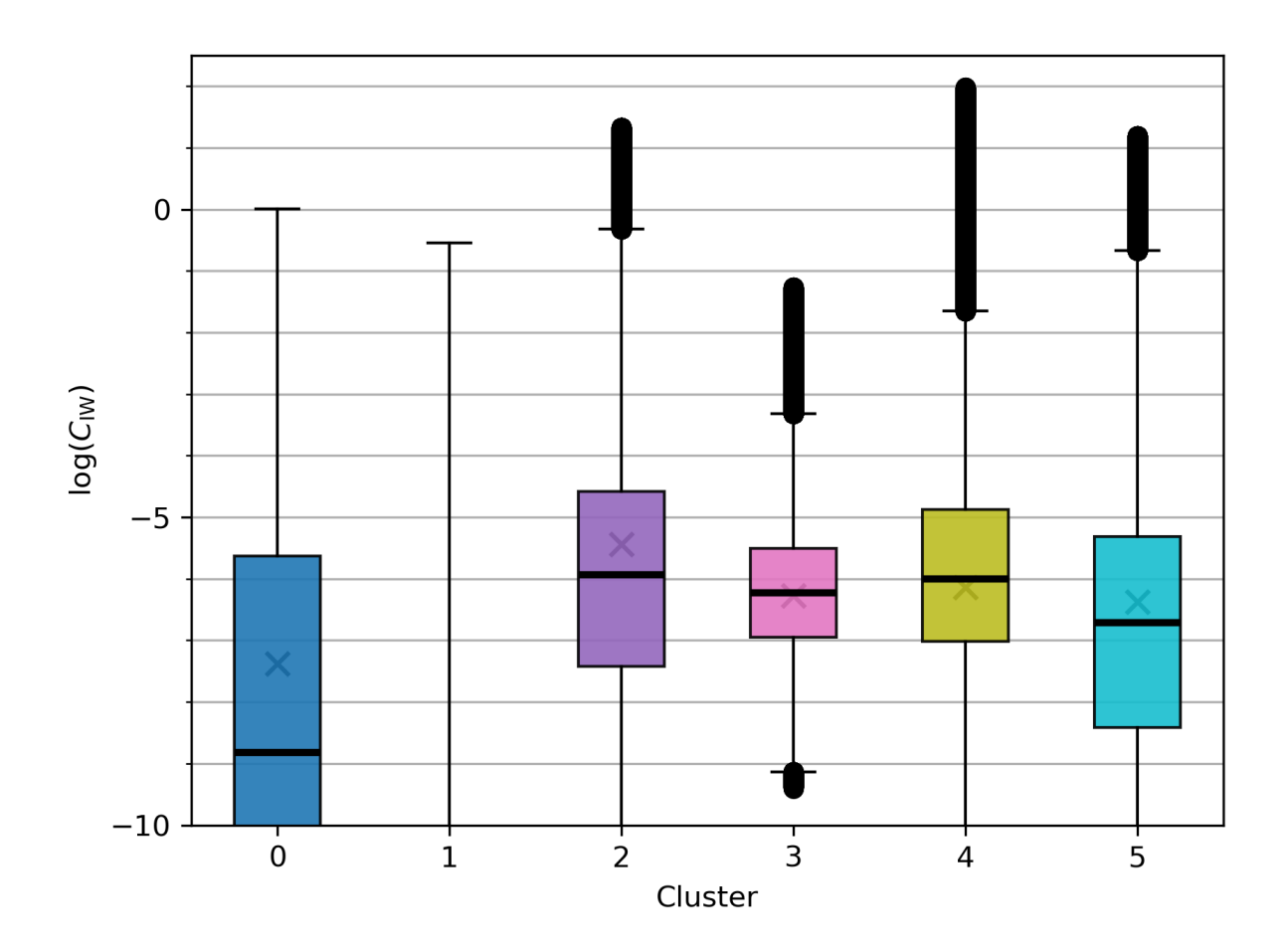


Figure 11. Distribution of internal wave drag  $C_{\rm IW}$  induced by the ice keel for each of the clusters based on annual-averaged data. For each cluster,  $C_{\rm IW}$  is computed using Eqns. (20)-(22) sweeping over the range of mean plus/minus two standard deviations for each nondimensional parameter. Mean and standard deviation of the distribution for each nondimensional parameter for each cluster are given in Table 1. Crosses indicate  $C_{\rm IW}$  values calculated using the mean value of each nondimensional parameter and correspond to the numerical simulations discussed in § 4.1. Note that values are presented on a logarithmic scale. In order to better see the differences across clusters with larger internal wave drag (clusters 2-5), the y-axis is cropped; values for cluster 1 predominantly fall below  $\log(C_{\rm IW}) = -10$  and are too small to be shown.

variables, but we re-write them here using the four nondimensional variables of interest:

390 
$$\Gamma(\chi,\zeta,\eta,\mathrm{Ri}) = \left(1 + \left(\frac{1}{\chi^2} + \mathrm{Ri}^2\right) \sinh^2(\pi\zeta\eta) - \mathrm{Ri}\sinh(2\pi\zeta\eta)\right)^{-1},\tag{21}$$

while the drag coefficient in a fully stratified (deep, non-mixed-layer) ocean is

395

405

$$C_{\text{DNW}}(\chi,\zeta) = \frac{\pi^2 \zeta^2}{2\chi} \sqrt{1-\chi^2}.$$
 (22)

This formulation, implemented in recent coupled ice—ocean models (e.g., Flocco et al., 2024), employs a set of interdependent nondimensional groups that jointly capture speed, geometry, and stratification rather than mapping one-to-one onto single processes. It reflects how variations in keel geometry, current speed, stratification, and mixed layer depth combine to regulate the efficiency of momentum transfer from drifting ice keels into the ocean interior.

Figure 10 maps how the parameterized internal-wave drag  $C_{\rm IW} = \Gamma \, C_{\rm DNW}$  varies across the explored parameter ranges.  $C_{\rm IW}$  increases with keel steepness  $\zeta$  [panels (a),(e)], decreases with increasing  $\eta$  (shallower keels relative to the mixed-layer depth) [panels (b),(d)], and decreases with  $\chi$  via  $C_{\rm DNW} \propto \sqrt{1-\chi^2}/\chi$  [panel (c)]. Sensitivity to Ri is weak at fixed  $\eta$  (nearly vertical contours in panels (c),(e)), but becomes pronounced through its coupling with  $\eta$ : small  $\eta$  and small Ri jointly maximize  $C_{\rm IW}$  [panel (f)]. Notably,  $\eta$  exerts strong leverage: as  $\eta \to 0$ ,  $C_{\rm IW}$  increases sharply, reflecting the efficiency of deeper keels in displacing the stratified ocean just beneath the ice; conversely, large  $\eta$  values imply keels that scarcely interact with the pycnocline, limiting wave generation. This scaling is consistent with the model behavior documented by Flocco et al. (2024), where shallow mixed layers elevate  $C_{\rm IW}$  by approximately an order of magnitude relative to deeper regimes.

Placing these theoretical parameterizations against the ranges of nondimensional parameters from the sea ice data in Figure 9, we observe that the canonical high-drag pocket — large  $\zeta$  with small  $\eta$  (Fig. 10(d)) — is sparsely populated by the annual- and winter-averaged ellipses, which concentrate at moderate  $\zeta \sim 0.1-0.3$  and  $\eta \sim 2-6$ . Figure 10 reveals additional high- $C_{\rm IW}$  pockets: (i) small  $\chi$  with large  $\zeta$  (panel (a)), (ii) small  $\chi$  across the full Ri range (panel (c), nearly vertical contours), and (iii) large  $\zeta$  across a wide Ri range (panel (e)). These pockets are not well-populated with data in the annual and winter distributions (Fig. 9 (a–f),(m–r)) but become pronounced in summer (Fig. 9 (g–l)), when the distributions shift toward larger  $\zeta$ , smaller  $\eta$ , and in some cases smaller  $\chi$ , thereby intersecting the regions of large  $C_{\rm IW}$  values.

Likewise, most annual winter data lie at intermediate  $\chi$  ( $\sim 0.3-0.5$ ), where  $C_{\rm IW}$  is not maximal, and at  ${\rm Ri} \sim 10^2-10^3$  together with  $\eta \sim 2-6$ , a regime where sensitivity to  ${\rm Ri}$  is weak at fixed  $\eta$  (Fig. 10 (c),(e)) and away from the small- $\eta$  and small- ${\rm Ri}$  ridge that maximizes  $\Gamma$  (Fig. 10(f)). Hence, while the theory predicts substantial drag for steep keels intersecting a shallow mixed layer, the states realized in the annual and winter distirbutions mostly occupy more moderate combinations, suggesting correspondingly moderate  $C_{\rm IW}$  in practice. By contrast, in summer several distributions intersects the large- $C_{\rm IW}$  pockets, which implies intermittent episodes of elevated drag that climatological means may underestimate.

The distribution of values of  $C_{\rm IW}$  for each cluster computed using Eqns. (20)-(22) based on the distribution of annually-averaged nondimensional numbers for each cluster projects that internal wave drag values span over several orders of magnitude (Fig. 11). Unsurprisingly, Clusters 0-1 with larger  $\eta$  (i.e., smaller ice keel depth relative to the mixed layer depth) have smaller  $C_{\rm IW}$ , which is consistent with the energetics metrics discussed in § 4.1. Crosses in Figure 11 correspond to the  $C_{\rm IW}$ 

values calculated using the mean values of the nondimensional variables for each cluster (see Table 1). According to this parameterization, ice keels with nondimensional number values of Cluster 2 induce the largest internal wave drag, about 5-10 times larger than those of Clusters 3-5. However, from our numerical simulations, we find that while the magnitude of kinetic energy  $E_K$  and kinetic energy dissipation rate  $\epsilon_K$  are proportionally amplified below the pycnocline for Cluster 2 compared to Clusters 3-5 (see Table 3), the overall magnitude of  $E_K$  and  $\epsilon_K$  are smaller everywhere (above, below, and around the pycnocline) for Cluster 2 (see Table 2). This suggests further investigation and potential adjustment of the parameterization of  $C_{\rm IW}$  through high-resolution numerical experiments is needed.

## 5 Conclusions

445

450

In our study, we combined upper ocean stratification parameters and keel characteristics, such as depth, spacing, and relative speed from the sea ice-ocean coupled NEMO-CICE model output (Flocco et al., 2024) into five nondimensional parameters to identify relevant ranges of values and parameter regimes of ice keel-ocean interactions. Specifically, we examined these parameters within the theoretical framework of McPhee and Kantha (1989) with a steadily moving ice keel along the surface of a two-layer upper ocean, such that an upper mixed layer is separated from the weakly stratified lower layer by a sharp pycno-cline. These nondimensional parameters captured (1) lee wave propagation potential in the stratified layer ( $\chi$ ), (2) nonlinearity of the waves (J), (3) steepness of the ice keel ( $\zeta$ ), (4) mixed layer depth relative to the keel depth ( $\eta$ ), and (5) the strength of the pycnocline relative to the flow shear (Ri).

Applying the GMM unsupervised clustering algorithm to these five nondimensional parameters allowed us to uncover statistically coherent clusters that potentially correspond to distinct dynamic environments. Clustering the time-averaged values of these five nondimensional parameters yielded six mechanically distinct and spatially-coherent sea ice regimes: boundarycurrent and margin regions (Clusters 0-2 in our analysis) versus more open-ocean conditions (Clusters 3-5 in our analysis from the central basin toward the shelves and marginal seas). The GMM fit used only nondimensional parameter values at each grid point (no geographic predictors), so the geographic coherence in our results reflects underlying mechanics rather than explicit location features. In order to assess the differences in resulting ocean flow dynamics, we also conducted high-resolution two dimensional numerical simulations using characteristic nondimensional parameter values for each of the six clusters. We found that in near-land boundary regions were likely to have less impact of the moving ice keels on the ocean flow and internal wave generation due to relatively not steep ice keel sides (Clusters 0 and 2) and relatively shallow keel depths compared to the mixed layer depth (Clusters 0 and 1). The simulations for the more open-ocean clusters (Clusters 3-5) exhibited larger kinetic energy magnitude and dissipation rates due to steeper and deeper ice keels (larger values of  $\zeta$ , J,  $\eta$ ), but the internal wave generation within and propagation into the stratified lower layer was stunted by the relatively large buoyancy jump across the pycnocline (large Ri). Interesting, moving from the center Arctic toward lower latitudes and into the marginal seas (Clusters  $3 \to 4 \to 5$ ), we found competing trends between (a) stabilizing effects that suppress internal wave generation and turbulence due to decreasing nonlinearity (mean values of  $J: 3.3 \rightarrow 2.4 \rightarrow 1.6$ ), keel steepness ( $\zeta: 0.31 \rightarrow 0.25 \rightarrow 0.17$ ), and relative keel depth ( $\eta: 2.0 \rightarrow 2.6 \rightarrow 5.1$ ), and (b) destabilizing effects that can boost internal wave propagation due to decreasing pycnocline strength (Ri:  $500 \rightarrow 290 \rightarrow 130$ ).

455

460

465

The results of this study also revealed the ranges of values for these five nondimensional parameters that are relevant to the Arctic sea ice. The parameterization (McPhee and Kantha, 1989) of internal wave drag  $C_{\rm TW}$ , which plays an important role in dissipating momentum in the upper ocean (Bouchat and Tremblay, 2014; Flocco et al., 2024), can expressed in term of these nondimensional parameters. With recent GPU-acceleration of computational fluid dynamics numerical codes (e.g., Oceananigans, il), Johnston et al. (2025) conducted a large numerical simulation sweep to test the existing parameterizations for the drag due to steady and tidal flows interacting with topographic obstacles along the ocean floor (i.e., seamounts). However, that problem has a different set of nondimensional parameters compared to the sea ice-flow interaction problem; namely, while rotation (the Coriolis parameter) does not play an important role for sea ice dynamics, additional nondimensional parameters to characterize the mixed layer depth  $(\eta)$  and buoyancy jump across the pycnocline (Ri) are relevant in the upper Arctic Ocean stratification, whereas constant stratification is assumed near the ocean bottom. Therefore, there is a need for similar studies with a consistent numerical set-up to test the existing sea ice drag parameterizations. Previous modeling efforts typically have only considered the variability of one or two of the relevant nondimensional parameters and only certain parameter regimes, e.g., only relatively deep ice keels ( $\eta = 0.25 - 2$  in Zhang et al. (2022) and De Abreu et al. (2024)) or in contrast, homogeneous fluid  $(\eta \to \infty)$  in Zu et al. (2021) and Wang et al. (2025)), whereas we find  $\eta$  to be in the range of [0, 140] and concentrated in the  $\eta \in [2,6]$  range. The values presented in this study are based on an ocean model output, and the spatio-temporal scales of the dataset are limited by the model resolution (e.g., the minimum mixed layer depth is 10 m). However, in the absence of well-distributed observational data of Arctic ice keel and near-surface ocean flow characteristics, our results provide a good starting point to consider for parameter sweeps in future numerical studies. Our results also suggest that certain joint ranges of parameter values might not need to be investigated in detail (e.g., large  $\chi$  and large  $\zeta$  combinations). This can in turn limit the number of numerical simulations to be run, which would allow for computational resources to be used to run additional simulations to test how physics that are neglected in the two-dimensional parameterizations, e.g., three-dimensional turbulence, three-dimensional effects due to flow splitting around the keel (Nikurashin et al., 2014) or ice keel sheltering effects (Wang et al., 2025), affect the dynamics of the flow and drag parameterizations.

Code and data availability. The code for the Oceananigans numerical simulations is available on Github (DOI: https://doi.org/10.5281/480 zenodo.17428925, repository url: https://github.com/bzemskova/2D\_seaice\_simulations.git) and the simulation outputs are available on Zenodo (DOI: https://doi.org/10.5281/zenodo.17428869). The code for clustering is available on Github (DOI:https://doi.org/10.5281/zenodo.17429505), repository url: https://github.com/fcliu03/Arctic\_Clustering.git

Author contributions. FL performed the GMM clustering and analysis. VEZ performed numerical simulations and analysis. The paper was primarily written by FL with supervision by VEZ.

Competing interests. The authors declare that they have no conflict of interest.

485

Acknowledgements. The authors acknowledge the support of the he Natural Sciences and Engineering Research Council of Canada. Numerical simulations were performed on the Nibi high-performance computing clusters supported by the Digital Research Alliance of Canada, Sharcnet, and Compute Ontario.

*Financial support.* This research has been supported by the Natural Sciences and Engineering Research Council of Canada (grant numbers: 490 RGPIN-2025-02281 and DGECR-2025-00478) and compute allocation from the Digital Research Alliance of Canada (RRG number 5443).

## References

- Baker, L. E. and Mashayek, A.: The Impact of Representations of Realistic Topography on Parameterized Oceanic Lee Wave Energy Flux, Journal of Geophysical Research: Oceans, 127, e2022JC018995, https://doi.org/https://doi.org/10.1029/2022JC018995, e2022JC018995 2022JC018995, 2022.
- 495 Bell Jr., T. H.: Topographically generated internal waves in the open ocean, Journal of Geophysical Research (1896-1977), 80, 320–327, https://doi.org/https://doi.org/10.1029/JC080i003p00320, 1975.
  - Bouchat, A. and Tremblay, B.: Energy dissipation in viscous-plastic sea-ice models, Journal of Geophysical Research: Oceans, 119, 976–994, 2014.
- Bouchat, A., Hutter, N., Chanut, J., Dupont, F., Dukhovskoy, D., Garric, G., Lee, Y. J., Lemieux, J.-F., Lique, C., Losch, M., et al.: Sea ice rheology experiment (SIREx): 1. Scaling and statistical properties of sea-ice deformation fields, Journal of Geophysical Research: Oceans, 127, e2021JC017 667, 2022.
  - Carmack, E. C., Yamamoto-Kawai, M., Haine, T. W. N., Bacon, S., Bluhm, B. A., Lique, C., Melling, H., Polyakov, I. V., Straneo, F., Timmermans, M.-L., and Williams, W. J.: Freshwater and its role in the Arctic Marine System: Sources, disposition, storage, export, and physical and biogeochemical consequences in the Arctic and global oceans, Journal of Geophysical Research: Biogeosciences, 121, 675–717, https://doi.org/10.1002/2015JG003140, 2016.
  - De Abreu, S., Cormier, R. M., Schee, M. G., Zemskova, V. E., Rosenblum, E., and Grisouard, N.: Two-dimensional numerical simulations of mixing under ice keels, The Cryosphere, 18, 3159–3176, https://doi.org/10.5194/tc-18-3159-2024, 2024.
  - Flocco, D., Feltham, D., Schroeder, D., Aksenov, Y., Siahaan, A., and Tsamados, M.: Impact of internal wave drag on Arctic sea ice, Annals of Glaciology, 65, e36, https://doi.org/10.1017/aog.2024.37, 2024.
- 510 Garrett, C. and Kunze, E.: Internal Tide Generation in the Deep Ocean, Annual Review of Fluid Mechanics, 39, 57–87, https://doi.org/https://doi.org/10.1146/annurev.fluid.39.050905.110227, 2007.
  - Huang, J., Pickart, R. S., Bahr, F., McRaven, L. T., Éric Tremblay, J., Michel, C., Jeansson, E., Kopec, B., Welker, J. M., and Ólafsdóttir, S. R.: Water mass evolution and general circulation of Baffin Bay: Observations from two shipboard surveys in 2021, Progress in Oceanography, 229, 103 322, https://doi.org/https://doi.org/10.1016/j.pocean.2024.103322, 2024.
- Hunke, E. C., Lipscomb, W. H., Turner, A. K., Jeffery, N., and Elliott, S.: CICE: the Los Alamos sea ice model documentation and software user's manual version 4.1 la-cc-06-012, T-3 Fluid Dynamics Group, Los Alamos National Laboratory, 675, 500, 2010.
  - Hutter, N., Bouchat, A., Dupont, F., Dukhovskoy, D., Koldunov, N., Lee, Y. J., Lemieux, J.-F., Lique, C., Losch, M., Maslowski, W., et al.: Sea ice rheology experiment (sirex): 2. Evaluating linear kinematic features in high-resolution sea ice simulations, Journal of Geophysical Research: Oceans, 127, e2021JC017666, 2022.
- 520 Johnston, D. R., Shakespeare, C. J., and Constantinou, N. C.: Evaluating and improving wave and non-wave stress parametrisations for oceanic flows, arXiv preprint arXiv:2503.12845, 2025.
  - Jones, D. and Ito, T.: Gaussian mixture modeling describes the geography of the surface ocean carbon budget., 2019.
  - Kanamitsu, M., Ebisuzaki, W., Woollen, J., Yang, S.-K., Hnilo, J., Fiorino, M., and Potter, G.: NCEP-doe amip-ii reanalysis (r-2), Bulletin of the American Meteorological Society, 83, 1631–1644, 2002.
- 525 Kawaguchi, Y., Itoh, M., Fukamachi, Y., Moriya, E., Onodera, J., Kikuchi, T., and Harada, N.: Year-round observations of sea-ice drift and near-inertial internal waves in the Northwind Abyssal Plain, Arctic Ocean, Polar Science, 21, 212–223, https://doi.org/https://doi.org/10.1016/j.polar.2019.01.004, iSAR-5/ Fifth International Symposium on Arctic Research, 2019.

- Kharitonov, V. V. and Borodkin, V. A.: On the results of studying ice ridges in the Shokal'skogo Strait, part I: Morphology and physical parameters in-situ, Cold Regions Science and Technology, 174, 103 041, https://doi.org/https://doi.org/10.1016/j.coldregions.2020.103041, 2020.
  - Klymak, J. M.: Nonpropagating Form Drag and Turbulence due to Stratified Flow over Large-Scale Abyssal Hill Topography, Journal of Physical Oceanography, 48, 2383 2395, https://doi.org/10.1175/JPO-D-17-0225.1, 2018.
  - Kolås, E. H., Fer, I., and Baumann, T. M.: The Polar Front in the northwestern Barents Sea: structure, variability and mixing, Ocean Science, 20, 895–916, https://doi.org/10.5194/os-20-895-2024, 2024.
- Korablev, A., Baranova, O. K., Smirnov, A. D., Seidov, D., and Parsons, A. R.: Climatological Atlas of the Nordic Seas and Northern North Atlantic, NOAA Atlas NESDIS 77, National Oceanographic Data Center (U.S.), https://doi.org/10.7289/V5K64G16, 2014.
  - Legg, S.: Mixing by Oceanic Lee Waves, Annual Review of Fluid Mechanics, 53, 173–201, https://doi.org/https://doi.org/10.1146/annurev-fluid-051220-043904, 2021.
- Mayer, F. and Fringer, O.: An unambiguous definition of the Froude number for lee waves in the deep ocean, Journal of Fluid Mechanics, 831, R3, 2017.
  - McPhee, M. G. and Kantha, L. H.: Generation of internal waves by sea ice, Journal of Geophysical Research: Oceans, 94, 3287–3302, https://doi.org/https://doi.org/10.1029/JC094iC03p03287, 1989.
  - Metzger, A. T., Mahoney, A. R., and Roberts, A. F.: The Average Shape of Sea Ice Ridge Keels, Geophysical Research Letters, 48, e2021GL095100, https://doi.org/https://doi.org/10.1029/2021GL095100, e2021GL095100 2021GL095100, 2021.
- Metzner, E. P. and Salzmann, M.: Technical note: Determining Arctic Ocean halocline and cold halostad depths based on vertical stability, Ocean Science, 19, 1453–1464, https://doi.org/10.5194/os-19-1453-2023, 2023.
  - Nikurashin, M. and Ferrari, R.: Radiation and Dissipation of Internal Waves Generated by Geostrophic Motions Impinging on Small-Scale Topography: Application to the Southern Ocean, Journal of Physical Oceanography, 40, 2025 2042, https://doi.org/10.1175/2010JPO4315.1, 2010.
- Nikurashin, M., Ferrari, R., Grisouard, N., and Polzin, K.: The Impact of Finite-Amplitude Bottom Topography on Internal Wave Generation in the Southern Ocean, Journal of Physical Oceanography, 44, 2938 2950, https://doi.org/10.1175/JPO-D-13-0201.1, 2014.
  - Notz, D. and Community, S.: Arctic Sea Ice in CMIP6, Geophysical Research Letters, 47, e2019GL086749, https://doi.org/https://doi.org/10.1029/2019GL086749, e2019GL086749 10.1029/2019GL086749, 2020.
  - Perfect, B., Kumar, N., and Riley, J. J.: Energetics of Seamount Wakes. Part II: Wave Fluxes, Journal of Physical Oceanography, 50, 1383 1398, https://doi.org/10.1175/JPO-D-19-0104.1, 2020.

555

- Ramadhan, A., Wagner, G., Hill, C., Campin, J.-M., Churavy, V., Besard, T., Souza, A., Edelman, A., Ferrari, R., and Marshall, J.: Oceananigans. jl: Fast and friendly geophysical fluid dynamics on GPUs, Journal of Open Source Software, 5, 2020.
- Rosenblum, E., Fajber, R., Stroeve, J. C., Gille, S. T., Tremblay, L. B., and Carmack, E. C.: Surface Salinity Under Transitioning Ice Cover in the Canada Basin: Climate Model Biases Linked to Vertical Distribution of Fresh Water, Geophysical Research Letters, 48, e2021GL094739, https://doi.org/10.1029/2021GL094739, e2021GL094739 2021GL094739, 2021.
- Selivanova, J., Iovino, D., and Cocetta, F.: Past and future of the Arctic sea ice in High-Resolution Model Intercomparison Project (High-ResMIP) climate models, The Cryosphere, 18, 2739–2763, https://doi.org/10.5194/tc-18-2739-2024, 2024.
- Silvestri, S., Wagner, G. L., Constantinou, N. C., Hill, C. N., Campin, J.-M., Souza, A. N., Bishnu, S., Churavy, V., Marshall, J., and Ferrari, R.: A GPU-based ocean dynamical core for routine mesoscale-resolving climate simulations, Journal of Advances in Modeling Earth Systems, 17, e2024MS004 465, 2025.

- Skyllingstad, E. D., Paulson, C. A., Pegau, W. S., McPhee, M. G., and Stanton, T.: Effects of keels on ice bottom turbulence exchange, Journal of Geophysical Research: Oceans, 108, https://doi.org/https://doi.org/10.1029/2002JC001488, 2003.
- Storkey, D., Blaker, A. T., Mathiot, P., Megann, A., Aksenov, Y., Blockley, E. W., Calvert, D., Graham, T., Hewitt, H. T., Hyder, P., et al.: UK Global Ocean GO6 and GO7: A traceable hierarchy of model resolutions, Geoscientific Model Development, 11, 3187–3213, 2018.
- Wagner, G. L., Silvestri, S., Constantinou, N. C., Ramadhan, A., Campin, J.-M., Hill, C., Chor, T., Strong-Wright, J., Lee, X. K., Poulin, F., et al.: High-level, high-resolution ocean modeling at all scales with Oceananigans, arXiv preprint arXiv:2502.14148, 2025.
  - Wang, S., Lu, P., Leppäranta, M., Zu, Y., Wang, Q., Li, Z., and Hao, P.: Sheltering of Sea Ice Ridges in the Ice-Ocean Drag Force: Implications From Idealized Laboratory Experiments, Journal of Geophysical Research: Oceans, 130, e2024JC020884, https://doi.org/10.1029/2024JC020884, e2024JC020884 2024JC020884, 2025.
- Winters, K. B. and Armi, L.: Hydraulic control of continuously stratified flow over an obstacle, Journal of fluid mechanics, 700, 502–513, 2012.
  - Ye, X. and Zhou, W.: Unsupervised Classification of Global Temperature Profiles Based on Gaussian Mixture Models, Journal of Marine Science and Engineering, 13, 92, https://proxy.lib.uwaterloo.ca/login?url=https://www.proquest.com/scholarly-journals/unsupervised-classification-global-temperature/docview/3159531269/se-2, copyright © 2025 by the authors. Licensee MDPI, Basel, Switzerland. This article is an open access article distributed under the terms and conditions of the Creative Commons Attribution (CC BY) license (https://creativecommons.org/licenses/by/4.0/). Notwithstanding the ProQuest Terms and Conditions, you may use this content in accordance with the terms of the License; Last updated 2025-07-24; SubjectsTermNotLitGenreText Southern Ocean; Environmental, 2025.

580

585

- Zemskova, V. E. and Grisouard, N.: Near-Inertial Dissipation due to Stratified Flow over Abyssal Topography, Journal of Physical Oceanography, 51, 2483 2504, https://doi.org/10.1175/JPO-D-21-0007.1, 2021.
- Zemskova, V. E. and Grisouard, N.: Energetics and mixing of stratified, rotating flow over abyssal hills, Journal of Physical Oceanography, 52, 1155–1177, 2022.
- Zhang, P., Xu, Z., Li, Q., You, J., Yin, B., Robertson, R., and Zheng, Q.: Numerical Simulations of Internal Solitary Wave Evolution Beneath an Ice Keel, Journal of Geophysical Research: Oceans, 127, e2020JC017 068, https://doi.org/https://doi.org/10.1029/2020JC017068, e2020JC017068, 2020JC017068, 2022.
- Zu, Y., Lu, P., Leppäranta, M., Cheng, B., and Li, Z.: On the Form Drag Coefficient Under Ridged Ice: Laboratory Experiments and Numerical Simulations From Ideal Scaling to Deep Water, Journal of Geophysical Research: Oceans, 126, e2020JC016976, https://doi.org/https://doi.org/10.1029/2020JC016976, e2020JC016976 2020JC016976, 2021.